UNIVERSITATEA DIN BUCUREȘTI

VIRTUTE ET SAPIENTIA

FACULTATEA DE FIZICĂ

An innovative architecture of Multi-Strip Multi-Gap Resistive Plate Counters for the inner zone of the Time-of-Flight system for the CBM experiment

Master's thesis

Daniel-Ion DOROBANŢU

Scientific Advisers:
Prof. Dr. Mihai PETROVICI
Dr. Mariana PETRIŞ
Prof. Dr. Mihaela SIN

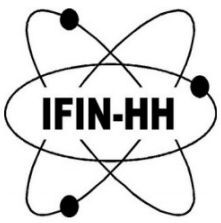

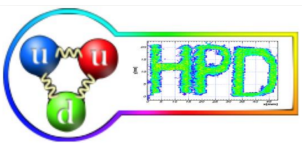

Bucharest, 2023

Acknowledgments

I would like to express my sincere thanks to my supervisor, Prof. Dr. Mihai Petrovici for his invaluable advice, continuous support and guidance and for always believing in me even when I did not believe in myself. I will forever remember every lesson he has ever taught me.

I am also grateful to Dr. Mariana Petriş for all her help, comments and suggestions and for always supporting me during my studies.

Also, I would like to thank Prof. Dr. Mihaela Sin for her unwavering support, guidance and advice.

This work was carried out under the contracts sponsored by the Romania Ministry of Research, Innovation and Digitalization: CBM FAIR-RO-03 (via IFA Coordination Agency) and PN-23-21 01 03.

Contents

Abstract

The understanding of the phase diagram of strongly interacting matter predicted by Quantum Chromodynamics (QCD) at high baryon chemical potential, where densities of the produced fireballs are 5-7 times higher than the normal nuclei, characteristic for the inner core of the neutron stars, requires a new generation of heavy-ion experiments. This could be achieved using high-intensity beams on a fixed target at low collision energies, where the properties and dynamics of highly compressed baryonic fireballs could be studied using high-performance detection systems.
The multi-differential analysis of the rare diagnostic probes and the understanding of the observed trends in the experimental data which can give a clue about the fundamental properties of the QCD matter require huge statistics. Therefore, a completely new heavy-ion experiment i.e. the future fixed target Compressed Baryonic Matter (CBM) experiment at the Facility for Antiproton and Ion Research (FAIR) in Darmstadt, designed to run at interaction rates of up to 10 MHz for Au-Au collisions at the energy available at the future SIS100 accelerator i.e. $\sqrt{s_{NN}} = 4.9\ GeV$ will shed light on the properties of highly compressed baryonic objects, where deconfined matter is produced, trying to study phase transitions which could occur and search for critical points of the QCD diagram.

The high-performance detection and identification systems of the CBM experiment have to maintain their performances in a very high counting rate environment over the whole lifetime of the experiment which is foreseen to run for 2 months a year for 10 years in order to perform high precision measurements and to ensure the quality of the experimental data.
Charged hadrons identification, mandatory for the understanding of the underlying physics, will be provided by the Time-of-Flight (ToF) system based on Multi-gap Resistive Plate Counters (MRPCs) and also using the momentum information of the produced particles measured with a tracking system placed in the magnetic field. At 8 meters from the target, at the low polar angles covered by the experiment i.e. at the inner zone of the CBM-ToF system, high particle densities with counting rates of up to $4 \cdot 10^4$ particles/$cm^2 \cdot s$ are expected. Therefore, the inner zone of the CBM-ToF system will be based on high counting rate, two-dimensional position sensitive, timing MSMGRPCs based on low resistivity glass.

Due to their operation in a very high irradiation dose, high-density avalanches lead to the ageing effects of the detectors which can affect their performance. In order to reduce the observed ageing effects, a completely new architecture of MSMGRPCs where the gas flow is directed through the gas gaps, leading to a higher gas exchange rate than the actual architecture where the gas exchange takes place via the diffusion process was developed as a mitigation solution of the ageing effects.
The detectors from the inner zone of the CBM-ToF system have to cope with different incident particle fluxes which have a strong dependence on the polar angle. In order to

fulfil the occupancy requirements which have to be below 5% which means to keep the probability of double hits as low as possible, the inner zone of the ToF system is based on 3 types of counters with different granularities i.e. 56/96/196 mm (strip length) $\times$ 300 mm.

The actual understanding of the phase diagram of strongly interacting matter predicted by Quantum Chromodynamics is presented in Chapter 1. A short description of the future CBM experiment designed to study the phase diagram of QCD matter can be seen in Chapter 2. Chapter 3 presents the time of flight method and the architecture of the CBM ToF system. Chapter 4 is dedicated to RPC (Resistive plate chamber) detector physics. Ageing tests for all 3 types of counters based on the new architecture at a realistic counting rate are reported in Chapter 5. The last chapter is dedicated to conclusions.

Chapter 1

The phase diagram of strongly interacting matter

Heavy-ion collisions at relativistic and ultrarelativistic energies are the only way to produce in the laboratory for a very short period of time (a few fm/c), in a very small volume deconfined matter also known as Quark-Gluon Plasma (QGP). The properties of strongly interacting matter are described by a non-Abelian gauge field theory called Quantum Chromodynamics (QCD) [1] which is a part of the Standard Model of Elementary Particles. One of the most important features of QCD matter is the asymptotic freedom i.e. the running coupling constant α_s is small at short distances, therefore partons (quarks and gluons) behave like free particles within a hadron and it becomes bigger at larger distances such that the partons are confined within hadrons. It follows that at high collision energy, the coupling constant decreases and quarks and gluons are expected to become free. Therefore, in a violent heavy-ion collision, it is expected to occur a phase transition from deconfined to confined matter [2].
Another feature of QCD matter is chiral symmetry which is spontaneously broken in the hadronic matter. The QCD Lagrangian exhibits chiral symmetry only for vanishing quark masses. Chiral phase transition is expected to occur in a very hot and dense medium which can be created using heavy-ion collisions.
The current understanding of QCD matter based on various theoretical studies [3],[4] implies the idea of a phase diagram which can be parameterized within the Statistical Model, using the grand canonical variables i.e. temperature T and baryonic chemical potential μ_B. Many experiments have been performed in order to study the phase diagram of strongly interacting matter, its phase transitions and search for its critical points.

One of the most important experiments is ALICE [5] (A Large Ion Collider Experiment) at CERN (Conseil Européen pour la Recherche Nucléaire) using the highest energy accessible at LHC (Large Hadron Collider) is designed to explore the Phase Diagram of Quantum Chromodynamics at very high temperatures and vanishing baryonic chemical potential. This could be achieved by colliding heavy ions accelerated at ultrarelativistic energies. At these extreme energies, colliding nuclei become transparent i.e. negligible stopping, therefore at mid-rapidity, the net baryon density is very small which implies a vanishing baryonic chemical potential, the number of particles being equal to the number of anti-particles produced in the collision. The theory predicts that the transition between Quark-Gluon Plasma and hadronic matter in this region of the phase diagram of QCD is a smooth crossover.

According to cosmological scenarios, a few microseconds after the Big Bang, our Universe was filled by this very hot matter i.e. Quark-Gluon Plasma, which is thought to be produced in fireballs of A-A collisions at ALICE experiment.

In the region of the phase diagram of QCD, at large baryonic chemical potential, it is expected to take place a first-order phase transition from Quark-Gluon Plasma to hadronic matter. It is believed that this first-order phase transition, at high temperatures, ends at a critical point which separates the crossover region from the boundary of the first-order phase transition. Based on various models, the critical point is predicted to be located at $T_E = 162 \pm 2$ MeV and $\mu_E = 360 \pm 40$ MeV [3].

In order to find the existence of the critical point, STAR (Solenoidal Tracker at RHIC) experiment at BNL (Brookhaven National Laboratory) using different energies accessible by the RHIC (Relativistic Heavy Ion Collider) accelerator, dedicated a program in order to scan the phase diagram of QCD at different baryonic chemical potentials i.e. BES I (Beam Energy Scan).
Colliding Au-Au at various energies, from $\sqrt{S_{NN}} = 200$ GeV to $\sqrt{S_{NN}} = 7.7$ GeV, it was a successful scan of the phase diagram from $\mu_B = 20$ MeV to $\mu_B = 420$ MeV. After the upgrade of the detection system, a fixed target program has been designed to perform a scan of the phase diagram i. e. BES II which will study with better statistics some regions of interest from the phase diagram [6].

A completely new experiment designed to explore the phase diagram predicted by Quantum Chromodynamics at very high baryonic chemical potentials i.e. $\mu_B > 500$ MeV and moderate temperatures is the future fixed-target CBM [7] (Compressed Baryonic Matter) experiment at FAIR (Facility for Anti-proton and Ion Research). Colliding heavy-ions at SIS100 (SchwerIonen Synchrotron) accelerator, where the synchrotron rigidity is 100 Tm, at beam energies up to 11A $\cdot$ GeV for Au ions ($\sqrt{S_{NN}} = 4.9$ GeV), at mid-rapidity, densities above $8\rho_0$, where ρ_0 is the saturation density of the nuclear matter ($\rho_0 = 0.17 fm^{-3}$) can be reached. In order to study the properties of the QCD matter populated at these tremendous densities, characteristic for the inner core of neutron stars, multi-differential analysis and high precision measurements of rare diagnostic probes are mandatory [8]. Aiming to fulfil these requirements, the CBM experiment is designed to run at unprecedented high interaction rates of up to 10 MHz for Au-Au collisions in order to achieve high statistics.

The phase diagram of strongly interacting matter predicted by Quantum Chromodynamics is depicted in Figure 1.1. As could be seen, Quantum Chromodynamics also predicts some exotic phases of matter such as Quarkyonic matter [9]. The point of coexistence of these three phases of matter is called the triple point. Statistical Model predicts that the triple point is located at $T_H = 150$–160 MeV and $\mu_H = 350$–400 MeV [3]. Another phase of matter predicted by QCD is colour superconductivity (CSC) which can be obtained at very large chemical baryonic potentials and small temperatures. At these huge densities and small temperatures, quarks can attract each other and it is believed to form Cooper pairs. Unfortunately, colour superconductivity (CSC) can not be studied using heavy-ion collisions because it is unlikely that this phase of matter to be produced in a heavy-ion collision.

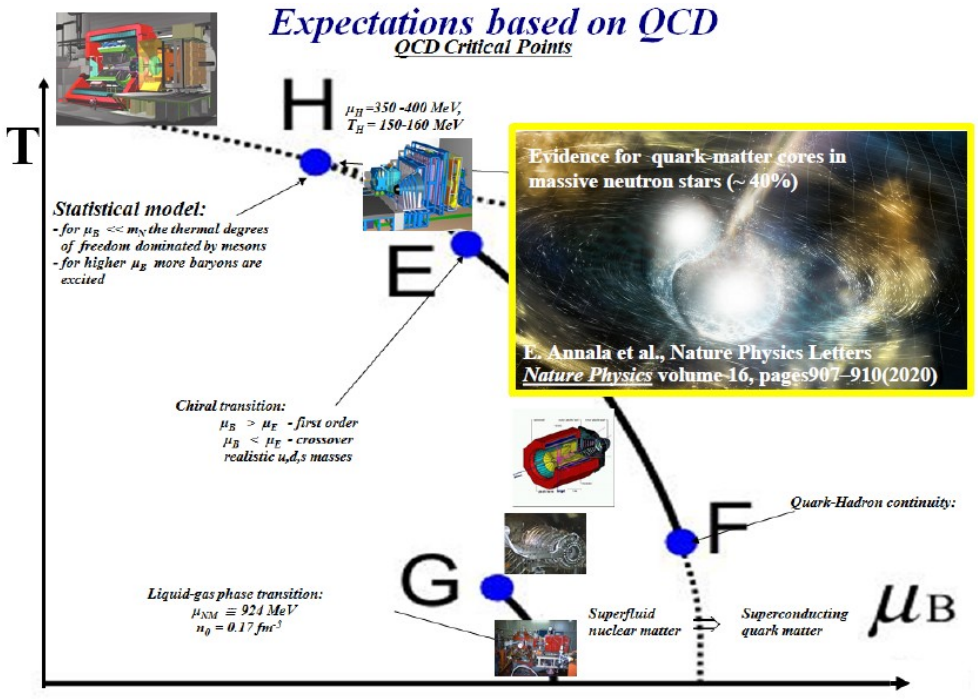

Figure 1.1: *The phase diagram of strongly interacting matter predicted by Quantum Chromodynamics.*

From the experimental point of view, the phase diagram predicted by QCD can be explored using heavy-ion collisions at various energies such to obtain different phases of matter populated at different temperatures and densities and after that to study their properties. In figure 1.2 it can be seen the dependence of the kinetic freeze-out temperature (on the left side) and the baryonic chemical potential (on the right side) of the Statistical Model as a function of the center-of-mass energy in a heavy-ion collision.

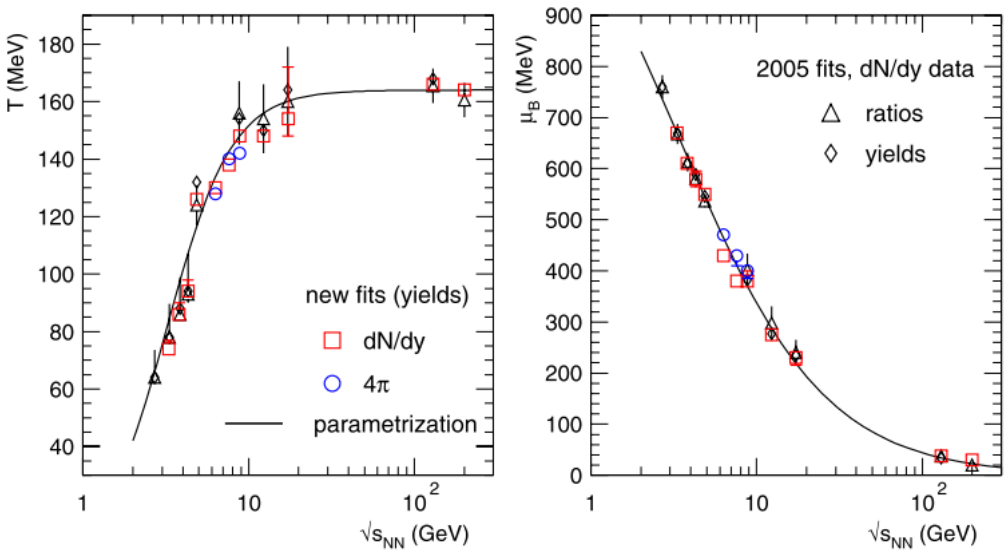

Figure 1.2: *The temperature T as a function of the center-of-mass energy (on the left side) and the baryonic chemical potential as a function of the center-of-mass energy (on the right side). Figures taken from [9].*

Chapter 2

The Compressed Baryonic Matter experiment

As mentioned already in the previous chapter, studying the phase diagram predicted by Quantum Chromodynamics at high baryonic chemical potentials and moderate temperatures, high precision measurements of the rare diagnostic probes and the understanding of the observed trends in experimental data require huge statistics. The future fixed-target CBM (Compressed Baryonic Matter) experiment at FAIR (Facility for Anti-proton and Ion Research) in Darmstadt, Germany, designed to run at unprecedented high interaction rates of up to 10 MHz for Au-Au collisions at beam energies up to 11 A $\cdot$ GeV ($\sqrt{S_{NN}} = 4.9$ GeV) will offer a unique opportunity to study the properties of QCD matter under extreme conditions.
Many experiments have been proposed in order to study the phase diagram of QCD at high baryonic potentials. Starting from AGS (Alternating Gradient Synchrotron) at BNL (Brookhaven National Laboratory), subsequent to RHIC and to higher energies at SPS (Super Proton Synchrotron) at CERN, different experiments have been dedicated in order to study the QCD matter at various baryonic potentials, search for phase transitions and critical points. An incredible amount of information has been achieved, but the properties of the deconfined matter obtained at high baryonic potentials still remain unclear.
For the understanding of the production mechanism of the deconfined matter, collision dynamics and time evolution of the system produced in heavy ion collisions have to be studied. The present view of heavy-ion collisions implies the idea of violent collisions between Lorentz contracted incident nuclei accelerated at velocities close to the speed of light. The very first stage after collision is called Glasma, which is a non-thermalised, highly in-homogeneous state with strongly interacting colour fields which is described within the Color Glass Condensate (CGC) framework. This state of matter lasts for about 0.1 fm/c. In the next stage of the collision, the system thermalises and the deconfined matter, or the so-called Quark Gluon Plasma, is formed, which lasts for a few fm/c after that the system undergoes a hydrodynamic expansion and a hadronization process. Being produced a highly in-homogeneous system, which lasts for a very short period of time, in a very small volume, which undergoes a hydrodynamic expansion and a hadronization process, the signals for deconfined matter, respectively for phase transitions and critical points are unclear [10].
In order to obtain information about the properties of very dense QCD matter, the CBM experiment will measure for the first time rare diagnostic probes from the early stages

of the collision, from the dense medium itself, produced in the heavy-ion collision, which have never been observed before at SIS100 energies [8]. These rare probes are very hard to be measured because of their low production cross section and the reconstruction of their invariant mass from a very high combinatorial background is challenging. In order to perform such an analysis, CBM will run at different interaction rates of up to 10 MHz. Previous experiments could not measure these rare probes because of the limitation of the rate capability of detector systems or luminosity of accelerators, therefore they did not achieve enough statistics for performing such type of measurements [7].
Figure 2.1 shows the interaction rates as a function of center-of-mass energy for ongoing and next-generation experiments. It can be seen that the CBM experiment is supposed to run at very high interaction rates of up to 10 MHz which have never been reached by other experiments.

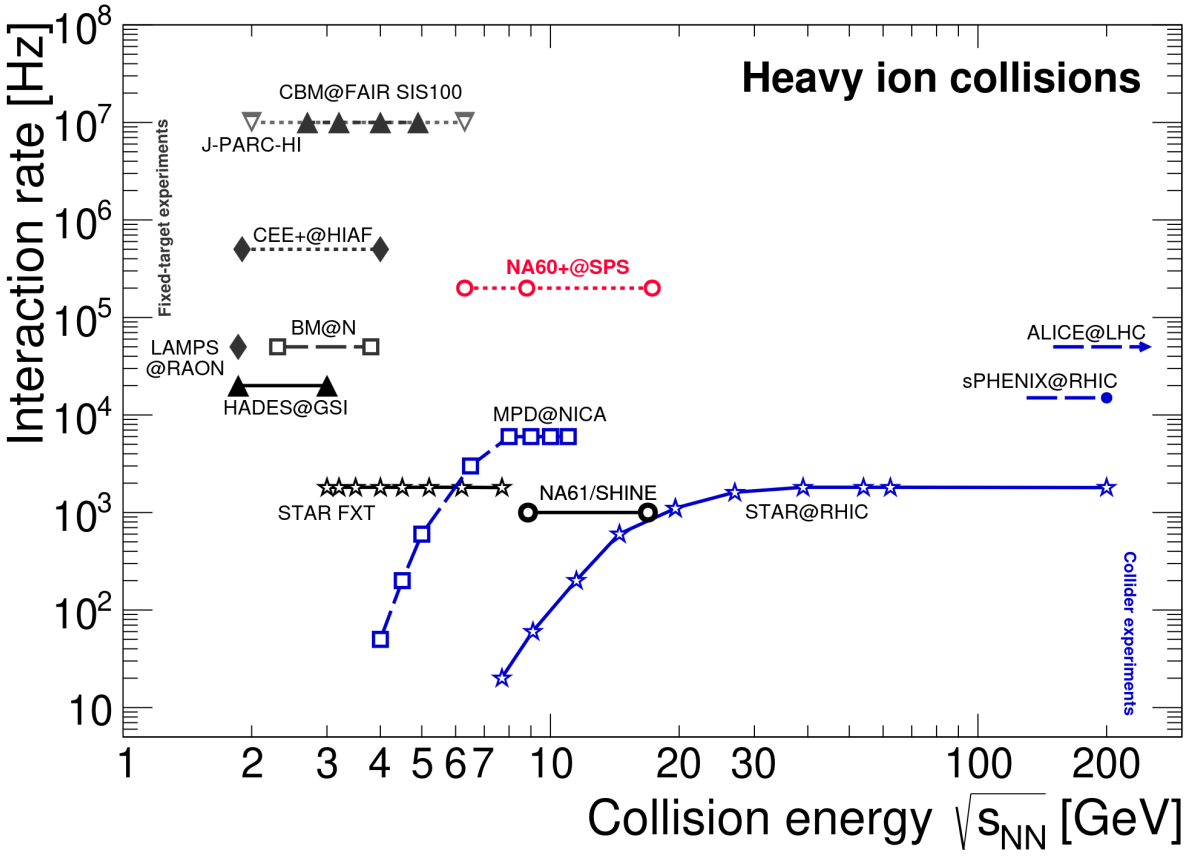

Figure 2.1: *The interaction rates of various experiments as a function of center-of-mass energy. Figure taken from [11].*

2.1 The physics motivation of the CBM experiment

The goal of the CBM experiment is to study the phase diagram at very high chemical baryonic potentials ($\mu_B > 500$), at densities characteristic of the inner core of neutron stars. Therefore, the CBM experiment will focus on the following problems:

- **The equation of state of QCD matter at very high densities**
  One way for studying the equation-of-state of the QCD dense matter is to measure

the collective flow of identified particles. Another promising way is to perform a measurement of the excitation function as a function of the multiplicity of multi-strange hyperons at beam energies covered by FAIR [7].

- **The properties of hadrons in dense medium and the idea of chiral symmetry restoration**
  According to QCD, a chiral phase transition is expected to occur in the dense medium. Because of chiral symmetry restoration, it is expected to appear a modification of the mass of hadrons. This could be studied by measuring the mass of vector mesons, in particular, ρ meson due to its short lifetime, therefore with a high probability, ρ meson will decay inside the dense medium. Because of the fact that dilepton does not interact through the strong force, they can give undisturbed information about the properties of the fireball in the initial stage of the collision, therefore the decay channel of ρ meson into dilepton is measured [12].
  It was pointed out by various theoretical studies [13] that the chiral fluctuations could be studied by measuring the momentum spectrum of the soft pions [14], where it is expected to be observed an enhancement of the yield of the soft pions. Therefore, studying the transverse momentum distributions at low p_T in order to understand the moat regime will give a clue about chiral critical point.

- **The phase transition from deconfined matter to the hadronic matter at high chemical baryonic potentials**
  Quantum Chromodynamics predicts that at high chemical baryonic potentials takes place a first-order phase transition from Quark-Gluon Plasma to hadronic matter which ends in a critical point. In order to find the critical point and to identify the phase transition, CBM will perform a measurement of the temperature of the initial fireball as a function of center-of-mass energy available at FAIR. The temperature of the initial fireball can be accessed by measuring the invariant mass of the lepton pair. If a caloric curve is obtained, it means that the theoretical predictions hold true [12].
  It is very well known that the baryonic number, charge and strangeness are conserved quantities in a heavy-ion collision. Studying higher-order cumulants of event-by-event fluctuations as a function of beam energy can give a clue about the existence of the critical point. The quantity $\kappa\sigma^2$, where κ is called kurtosis of the multiplicity distribution, of conserved quantities, is found to exhibit a non-monotonic behaviour in the vicinity of the critical point[7].

- **The study of multi-strange hyper-nuclei and looking for exotic strange objects**
  According to the Statistical Model, the production cross section for hyper-nuclei have a maximum of around 10 A $\cdot$ GeV, energy covered by FAIR. More challenging is the measurement of double-Λ hyper-nuclei and their lifetime.

- **The study of charm particles produced close to the threshold**
  In a heavy-ion collision, charm particles are produced at the very first stage of the collision. At SIS100 energies the production of charm particles is near the threshold. Therefore, CBM will study the properties of the charm particles that are produced near the threshold [7].

2.2 Facility for Anti-proton and Ion Research

At GSI Helmholtzzentrum für Schwerionenforschung [15] in Germany, Darmstadt will be built a new facility for research in nuclear physics called FAIR (Facility for Anti-proton and Ion Research). At FAIR, the main accelerator is a synchrotron with a rigidity of 100 Tm called SIS100 (SchwerIonen Synchrotron), which have a circumference of 1100 m. Particles provided by the ion source are accelerated by the UNILAC accelerator (Universal Linear Accelerator) which has 120 m length, at velocities up to 20% of the speed of light after that particles are injected into the SIS18 accelerator which has a circumference of 216 meters where particles are accelerated at velocities up to 90 % of the speed of light. The SIS18 accelerator will serve as an injector in the future SIS100 synchrotron. An image of the experimental arrangement of FAIR is depicted in Figure 2.2.

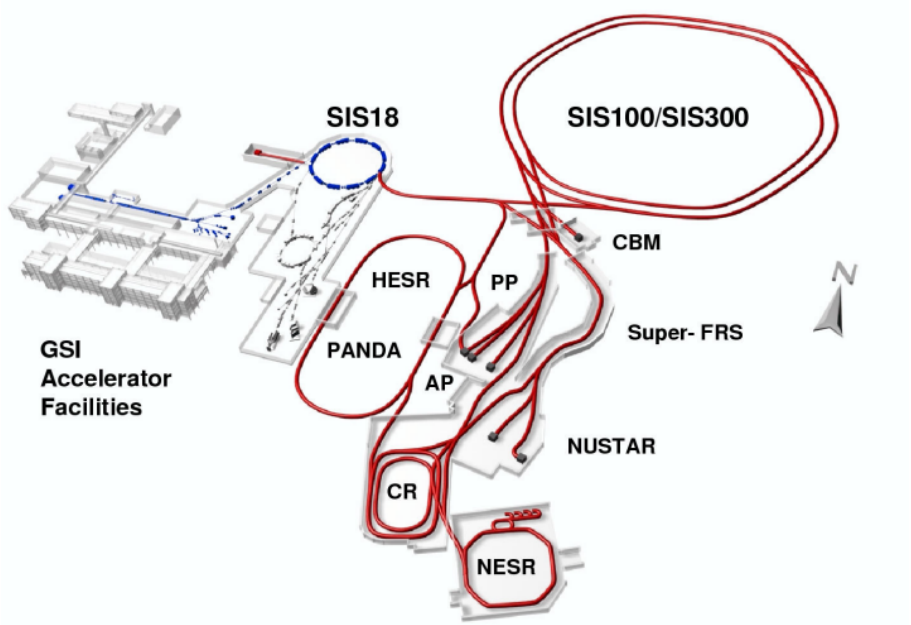

Figure 2.2: *Facility for Anti-proton and Ion Research. Figure taken from [16].*

The beam is delivered by the SIS100 to the CBM experiment with intensities up to 10^9 Au ions per second. Table 2.1 shows the maximum energy at which ions can be accelerated by the SIS100 accelerator.

Table 2.1: *Beam energy at the SIS100 accelerator [8].*

Beam	**Z**	**A**	**E/A GeV at SIS100**
p	1	1	29
d	1	2	14
Ca	20	40	14
Ni	28	58	13.6
In	49	115	11.9
Au	79	197	11
U	92	238	10.7

2.3 The design of the CBM experiment

The CBM experiment was designed to cope with interaction rates of up to 10^7 events/s, with a multiplicity of up to 1000 charged particles per event for Au-Au collisions. Due to kinematic focusing, produced particles in the collision are emitted in the forward direction, therefore detectors have to have high rate capabilities in order to detect all incident particles. The CBM experiment is supposed to run 2 months/year for about 10 years in an unprecedentedly high counting rate, hence the detectors used in the experimental arrangement have to be designed such that to maintain their performances over the whole lifetime of the experiment and the ageing effects due to high irradiation dose environment to be reduced at maximum. The acceptance of the CBM detection system for the polar angles starts from 2.5° up to 25° and the azimuth angle is almost 2π [16]. For studying the properties and dynamics of high-density fireballs, the detection system of the CBM experiment has to be able to identify both hadrons and leptons. Two experimental arrangements of the CBM detection system have been proposed for measuring rare diagnostic probes. The detection system of the CBM experiment is depicted in Figure 2.3. It shows the two configurations of the detection system of the CBM experiment. The first configuration of the detection system is focused on electron measurements and the second configuration is focused on muon measurements [12].

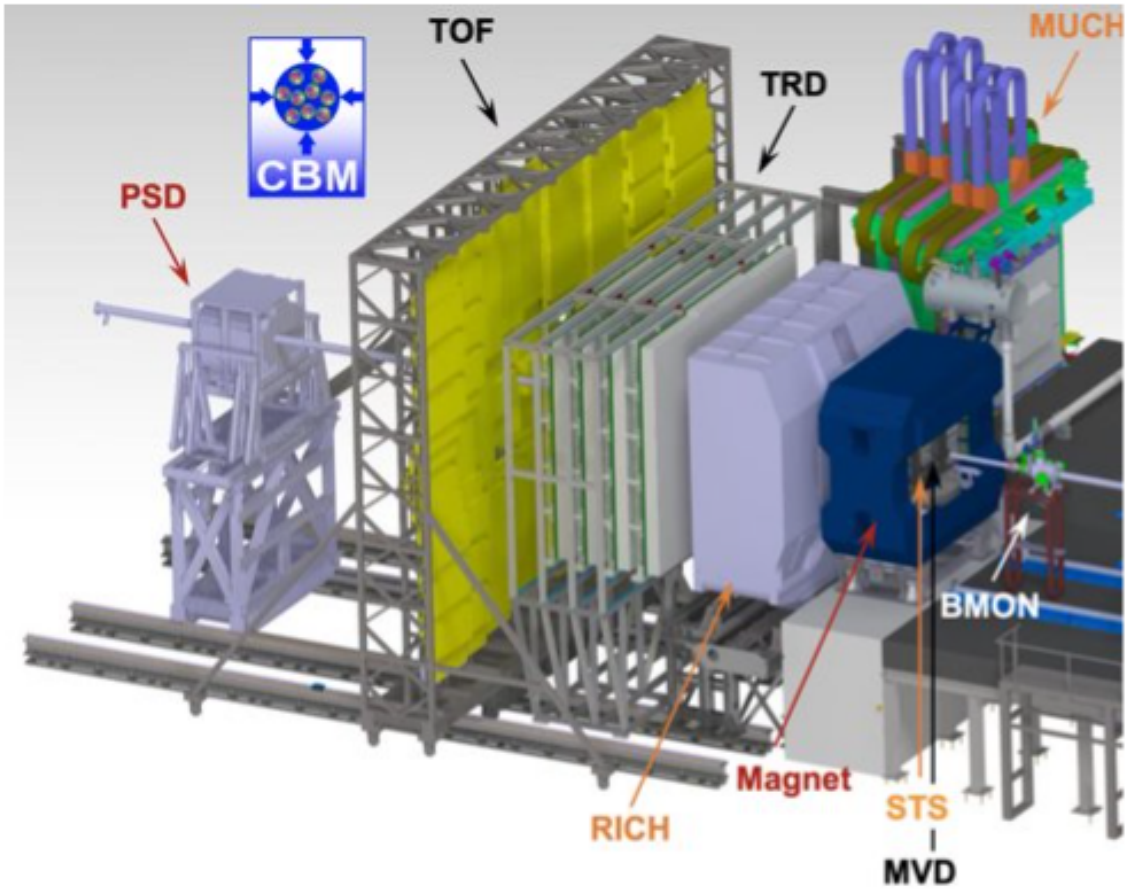

Figure 2.3: *The CBM experiment. Figure taken from [17].*

- **Magnet**
  A very important step towards identifying charged particles produced in a collision is the determination of the momentum of these particles. Measuring the curvature of charged particles in a magnetic field can provide information about their momentum. The magnet for the CBM experiment[18] is a superconducting dipole magnet which provides a maximum magnetic field of up to 1 T. The measurement of the momentum of charged particles has a very good resolution, about $\Delta p/p = 1\%$. The polar angle acceptance of the magnet is about $\pm 25°$. The coils are cooled using a circuit filled with liquid Helium at 4.5 K. The sketch of the magnet is depicted in Figure 2.4.

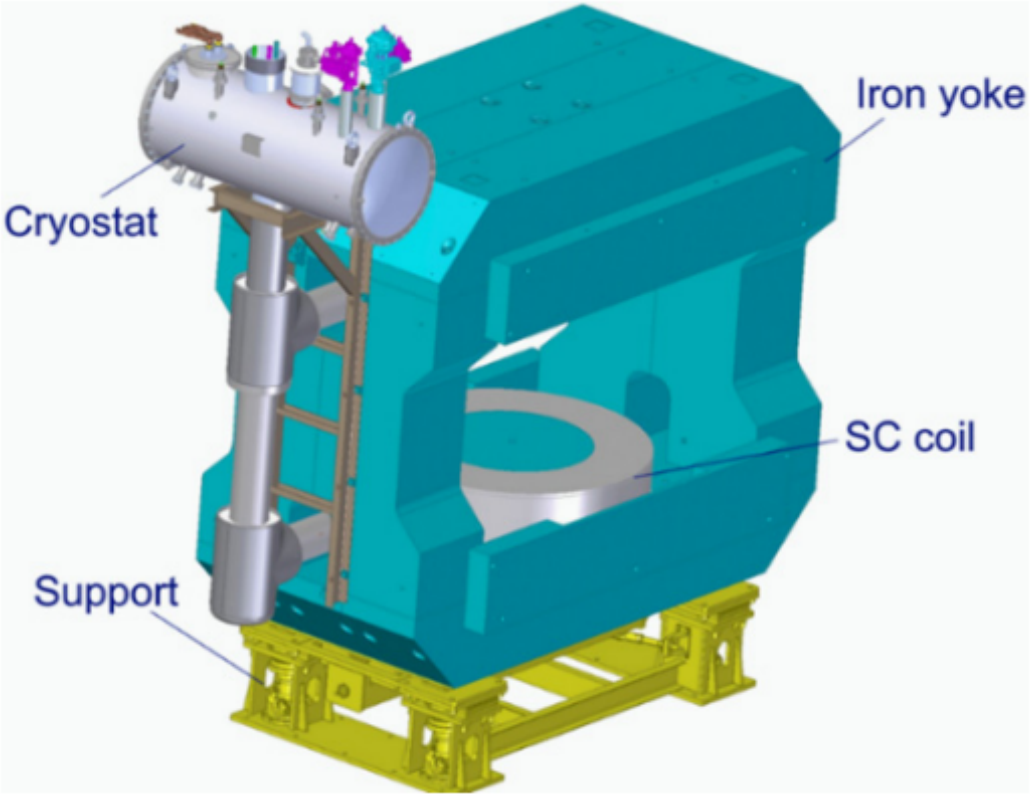

Figure 2.4: *The sketch of the dipole magnet for the CBM experiment. Figure taken from [19].*

- **Micro-Vertex Detector**
  The Micro-Vertex Detector (MVD) [20] based on MIMOSIS which is a monolithic active pixel sensor, will have four stations and will be placed in the vacuum, in the magnetic field, at 5 to 20 cm downstream of the target. The goal of the MVD detector is to reconstruct the secondary vertex of particles which have a very short time life i.e. D mesons which decay via weak interaction into pions and kaons. The MVD detector can be used for background rejection of electron-positron pairs from gamma photon conversions such that to improve the signal-to-background ratio. It has a very good position resolution of about $50 - 100$ μm, therefore it can be used for tracking, complementary to the STS detector to suppress spurious tracks. Also, using the missing mass method, it can be used for the reconstruction of the particles which decay into one neutral daughter particle such as Λ hyperons. It can be seen a sketch of the MVD detector in Figure 2.5.

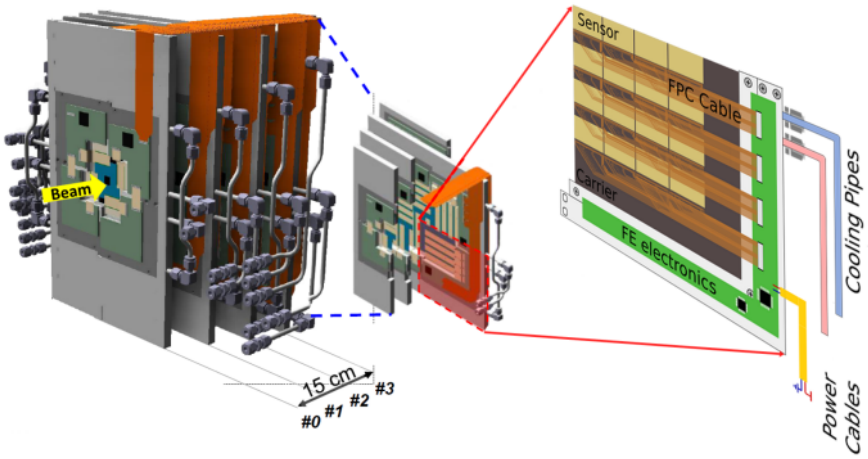

Figure 2.5: *The sketch of the MVD detector. On the left side, it is showed the MVD detector with four stations and on the right side, it is a zoom of one station. Figure taken from [20].*

- **Silicon Tracking System**
  The Silicon Tracking System (STS) [21] is placed in the magnetic field and it has to measure the momentum of charged particles with a very good resolution of about $\Delta p/p = 1\%$. Being the main tracking detector it has to measure trajectories of charged particles produced in the collision, therefore an efficiency above 95% for track reconstruction is required. At interaction rates of up to 10^7 Hz, up to 1000 charged particles are produced per event for Au-Au collisions. In order to fulfil these requirements, an architecture of a detector based on silicon micro-strip sensors has been chosen. Eight layers of silicon micro-strip sensors, with a very low material budget, placed at 30 cm to 100 cm downstream of the target in the magnetic field, kept at a constant temperature of up to $-5°C$ will provide track reconstruction and momentum determination for all charged particles produced in the collision. A sketch of STS stations can be seen in Figure 2.6.

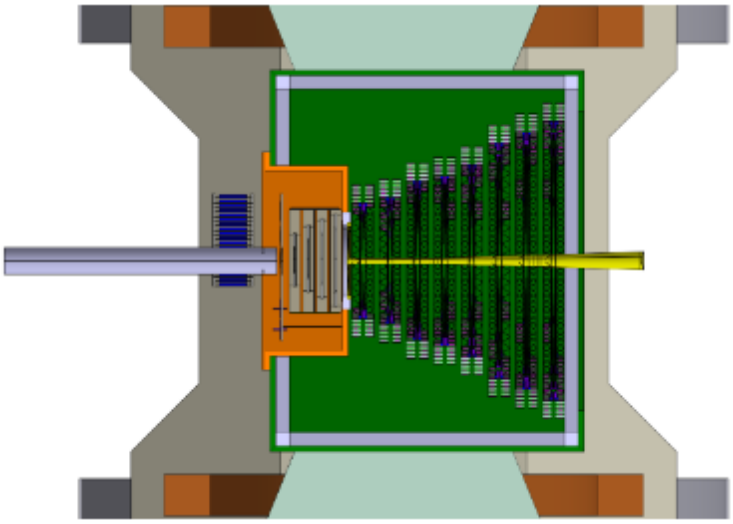

Figure 2.6: *The sketch of the STS detector which is placed inside the magnetic field integrated with MVD detector. Figure taken from [21].*

- **Ring-Imaging Cherenkov Detector**
  The Ring Imaging Cherenkov Detector (RICH) [22] will identify both electrons and pions with momenta up to 10 GeV/c using Cherenkov radiation emitted by electrons and pions in a gaseous radiator i.e. CO_2 which have a refractive index n = 1.00045 measured at T =0°C and p = 1 atm, therefore the threshold momentum for pions in the radiator is p_{thr} = 4.65 GeV/c and the maximum Cherenkov angle $\theta_C^{max} = 1.72°$. The pion suppression factor has to be at least 100 in order to measure with high-precision di-electrons probes. The Cherenkov photons are reflected on two arrays of spherical glass mirrors. The Cherenkov rings are reconstructed on two-photon detectors based on multi-anode photomultipliers (MaPMT). The invariant mass of a particle can be reconstructed by measuring the radius of the Cherenkov ring and the momentum of the charged particle. The sketch of the RICH detector is depicted in Figure 2.7.

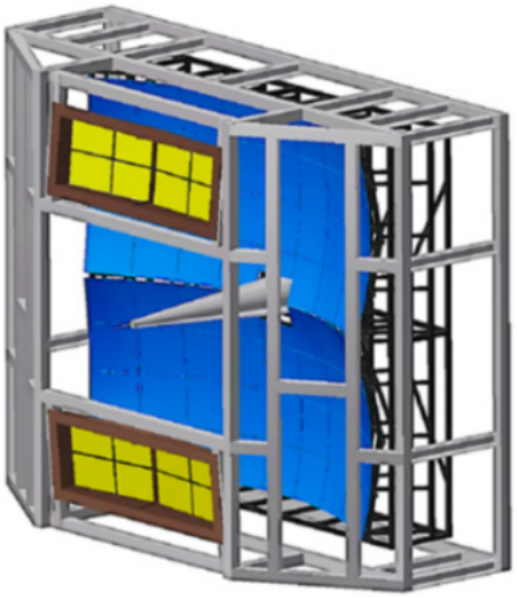

Figure 2.7: *The sketch of the RICH detector. Figure taken from [19].*

- **Muon Chamber System**
  The Muon Chamber System (MuCh) [23] will identify muon pairs which are very important diagnostic probes for the physics case of the CBM experiment. It will be a challenging task for the muon detection system to identify low momenta muon pairs from a very high combinatorial background at SIS100 energies. These types of measurements have never been performed at such low collision energies, therefore MuCh system has been designed to identify soft muons which carry invaluable information about the properties of the fireball [12]. Pairs of three tracking detector layers are placed in-between hadron absorber plates, the first of them made of carbon and the others made of iron of different thicknesses. At the highest interaction rates of up to 500 kHz/cm^2 tracking detectors are based on GEM (Gas electron multiplier) architecture. At interaction rates around 15 kHz/cm^2 which will be reached at the third station and 4 kHz/cm^2 for the fourth station, RPC (Resistive plate chamber) detectors with one gas gap have been chosen as the tracking detector. A sketch of the MuCh system can be seen in Figure 2.8.

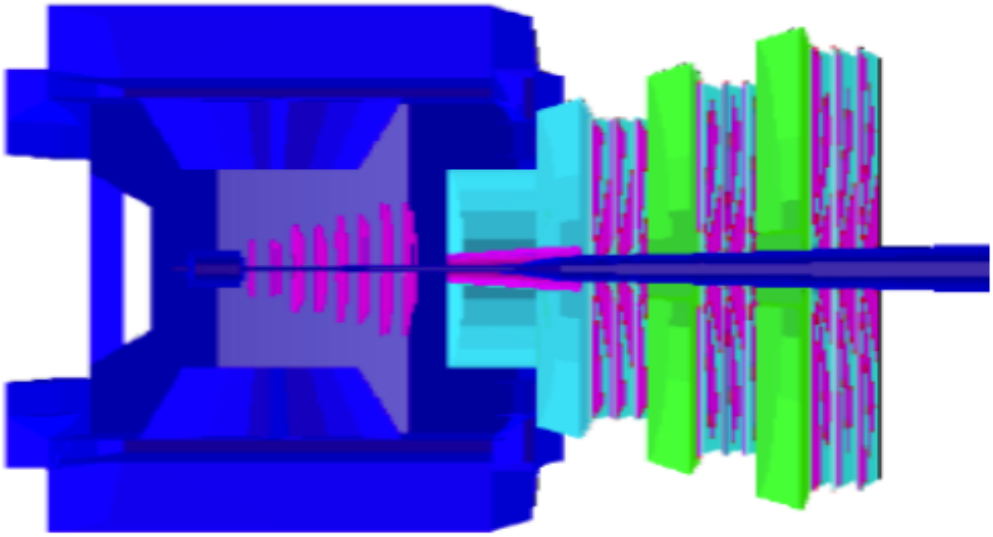

Figure 2.8: *The sketch of the MuCh detector. Figure taken from [23].*

- **Transition Radiation Detector**
  The Transition Radiation Detector (TRD) [24] will identify electrons with $\gamma > 1000$ at an efficiency of 90% and the pion rejection factor has to be > 100 for a good signal-to-background ratio in order to measure dielectrons which are extremely important for the physics case of the CBM experiment. Therefore, it will extend the electron identification capability of the RICH system above the momenta of 5 GeV/c. This can be achieved using transition radiation which is emitted in the very forward direction ($\theta \propto 1/\gamma$) when a relativistic charged particle (electron) crosses the boundary between two media which have different refraction indices (the radiator). The energy of the transition radiation photons is in the order of 10 keV being in the X-ray range, therefore the entrance window of the TRD has to be optimized such that to have minimal absorption for the transition radiation (TR) photons in order to achieve the expected performances [25] .
  It will be placed between the STS and ToF system and being a tracking detector, it will reduce the track mismatches between the STS and ToF system, hence it will enhance the PID performance. Also, it will identify charged nuclear fragments via their specific energy loss for example hyper-nuclei.
  The TRD system is based on Multi Wire Proportional Chambers (MWPC) and it has one station with 4 layers. The radiator will be placed in front of the chambers. The TRD uses as readout rectangular pads which have a spatial resolution of 300 μm across the pads and provide one-dimensional position information. In order to reconstruct the spatial position in 2 dimensions every second parallel layer has to be rotated by 90°. In order to measure p_T spectra of very low values around 100 MeV /c in a very high counting rate environment of up to 100 kHz/cm^2 at the small polar angles, the inner zone of the TRD system will be based on a completely new detector concept which can provide two-dimensional position information using just one layer i.e. TRD-2D [14]. This could be achieved using as readout electrodes a combination of triangular pads instead of rectangular pads. The position resolution of the TRD-2D is in the order of 100 μm across pads. A sketch of the TRD system is depicted in Figure 2.9.

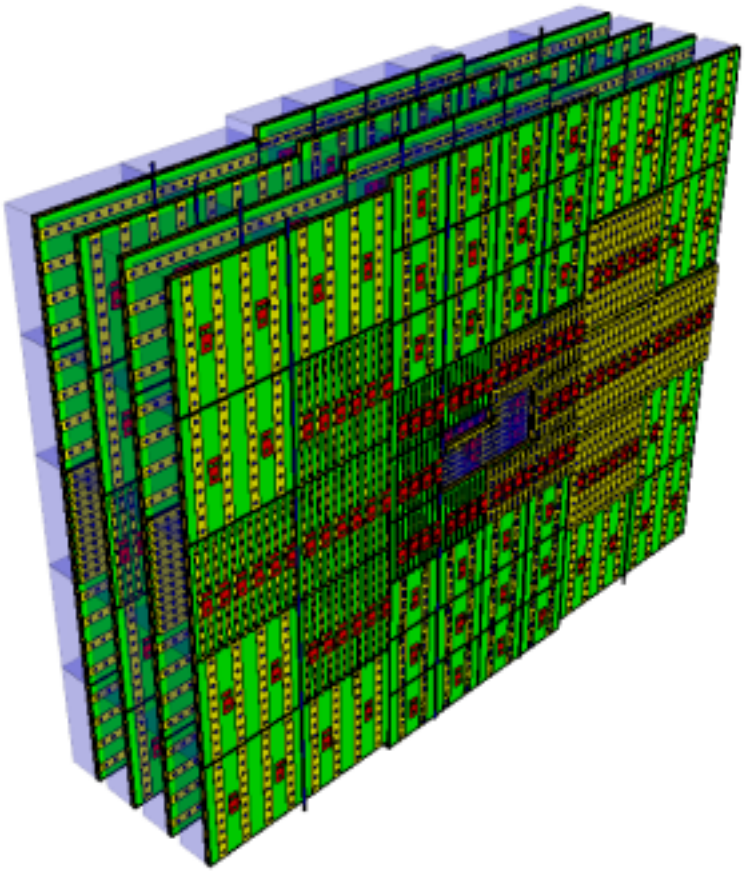

Figure 2.9: *The sketch of the TRD system. It is depicted a station with 4 layers. Figure taken from [24].*

- **Time-of-Flight System**
  The Time-of-Flight System (ToF) [16] will measure the time of flight of charged hadrons produced in collisions and using the information about their momenta from their curvature in the magnetic field measured by the STS system will identify these hadrons. Therefore, the ToF system can identify only particles that were found by the STS system and for this reason, tracks from STS have to be extrapolated and matched with hits in the ToF system. Hence, the ToF system has to cover the STS acceptance i.e. polar angles starting from 2.5° to 25°. The ToF system will be placed at different distances i. e. from 6 m to 10 m from the target in order to optimize the PID performance for the experimental setup accordingly to the type of measurement. It has an active area of about 120 m^2.
  Detectors used by the ToF system have to have a system time resolution better than 80 ps and an efficiency over 95%. In order to fulfil these requirements ToF system is based on timing MRPC (Multi Gap Resistive Plate Chambers) detectors. The incident flux of charged hadrons has a strong dependence on the polar angles, therefore detectors with different rate capabilities and granularities are needed. In the inner zone of the ToF wall, where the incident particle flux can reach 40 kHz/cm^2, MRPC based on low resistivity glass are the best option.
  Figure 2.10 shows a sketch of the ToF system.

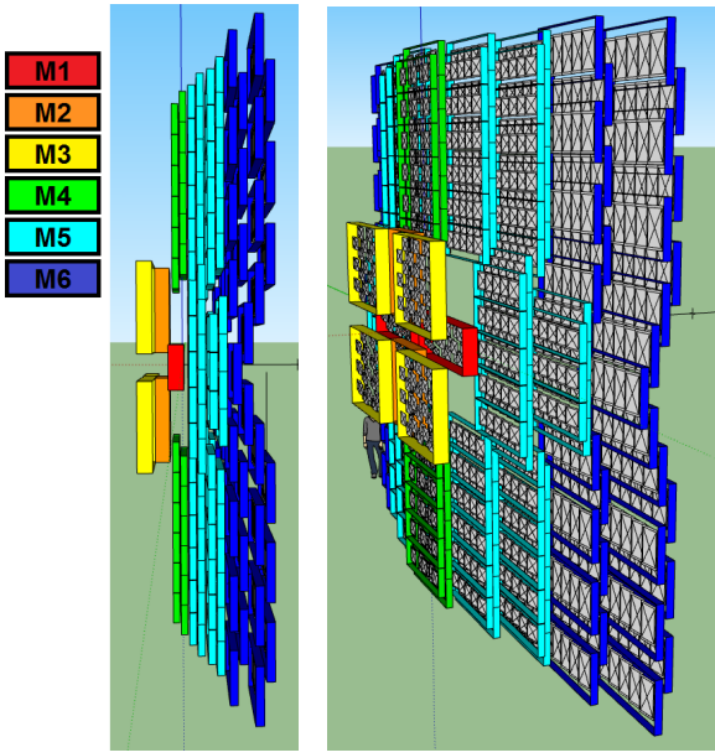

Figure 2.10: *The sketch of the ToF system. Figure taken from [16].*

- **Electromagnetic Calorimeter**
  The Electromagnetic Calorimeter (ECAL) [26] will measure the energy of photons, neutral mesons which decay into photons (π^0, η) and it also can identify electrons. It is a sampling calorimeter which has 140 layers of alternating 1 mm scintillator readout by photomultipliers and 1 mm lead.

- **Projectile spectator detector**
  The Projectile spectator detector (PSD) [27] is a compensating hadronic calorimeter based on 60 lead/scintillator layers readout by micropixel avalanche photodiodes (MAPD). The goal of the PSD detector is to determine collision centrality by measuring the spectator fragmentation, therefore it can be determined the impact parameter b and the orientation of the reaction plan.

Chapter 3

The Time-of-Flight System

Charged hadrons identification will be provided by the Time-of-Flight (ToF) system which will measure the arrival time of the charged hadrons produced in the collision. In order to identify a particle using the time-of-flight method, the momentum of this particle is determined using the STS system which is placed in the magnetic field which allows momentum determination from the curvature of this particle in the magnetic field. Being a tracking detector, the STS system can also reconstruct tracks of particles which are extrapolated to an intermediate tracker detector between STS and ToF i.e. the Transition Radiation Detector (TRD) and finally, these tracks are matched to the nearest hit in the ToF detectors. Therefore, the ToF system has to cover the STS acceptance i.e. polar angles starting from 2.5° up to 25°.
The CBM experiment will run at interaction rates of up to 10 MHz for Au–Au collisions at $\sqrt{s_{NN}}$ = 2–5 GeV, hence due to kinematic focusing, at the lowest polar angles, the incident charged particle flux up to $4 \cdot 10^4$ $particles/cm^2 \cdot s$ and 1 hit/ cm^2 at the ToF wall, placed at 8 m from the target are expected.
In order to detect and to perform a qualitative PID i.e. to distinguish kaons from pions and protons, the requirements for the detectors of the ToF system are to provide a system time resolution better than 80 ps, an efficiency over 95% and an occupancy below 5% with a minimum number of readout channels. Detectors which fulfil these requirements are timing MRPCs (Multi-Gap Resistive Plate Chambers).

Figure 3.1 shows a simulation of the incident flux of charged particles for Au–Au collisions at E = 11 A · GeV at an interaction rate of 10 MHz at a distance of 8 m from the target. It can be seen that the incident particle flux at the ToF wall has a strong dependence on the polar angle, therefore the architecture of the CBM-ToF wall is based on detectors with different rate capabilities and granularities in order to maintain the requirements needed for performing a qualitative PID.
Detectors from the inner zone of the ToF wall, where the incident particle flux can reach 40 kHz/cm^2, are double stack HV MRPC counters and are based on low resistivity glass electrodes with 10 gas gaps [16]. The ToF system has a modular architecture with 6 types of modules and it covers an area of about 120 m^2. In order to avoid dead zones, modules and detectors from modules are overlapped in such a way as to assure a continuous active area.

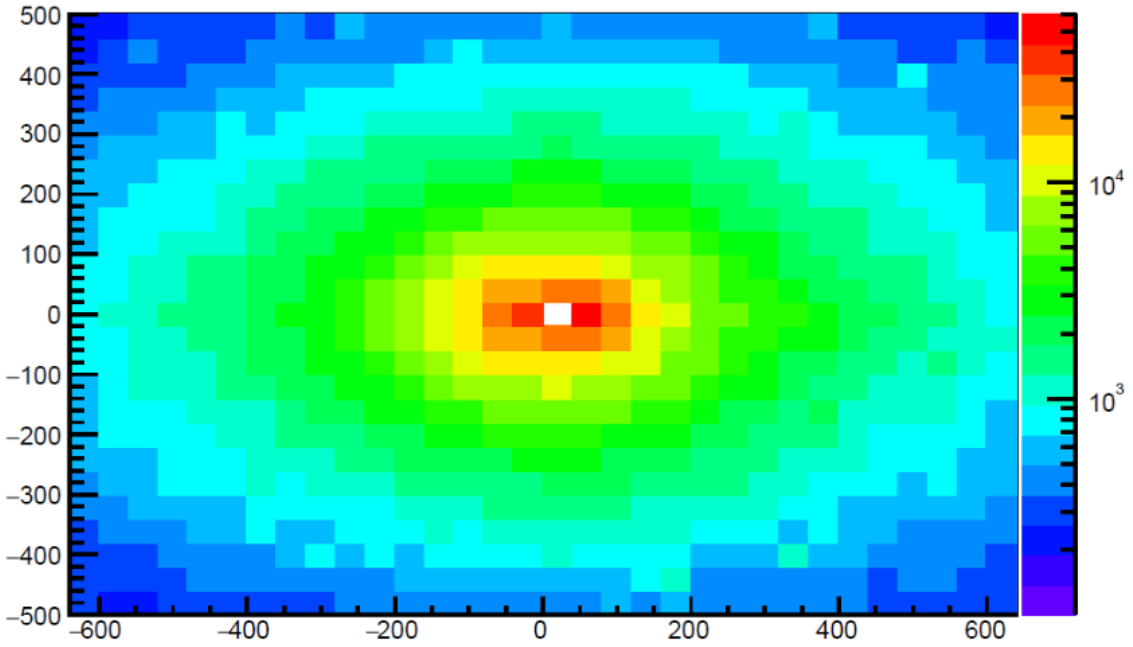

Figure 3.1: *FLUKA simulation of the incident flux of charged particle for Au–Au collisions at $E = 11\ A \cdot GeV$ at an interaction rate of 10 MHz at a distance of 8 m from the target. It can be seen that the incident particle flux has a strong dependence on the polar angle. Figure taken from [28].*

3.1 The time-of-flight method

The goal of any PID method is to identify a certain particle. This could be achieved either by reconstructing the invariant mass of a particle or by analyzing the way in which it interacts in different types of detectors. All charged hadrons have the same type of interaction, therefore the only way to identify them is using the so-called PID by mass determination method [29]. One of the best ways to reconstruct the invariant mass of charged hadrons is the time-of-flight method [30]. The idea behind this technique is to measure the time taken for a particle to fly over a given path length, from a start to a stop detector. A sketch of this principle is depicted in Figure 3.2.

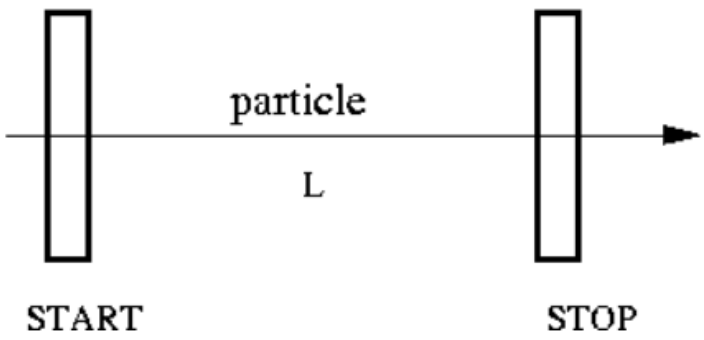

Figure 3.2: *The sketch shows the start-stop system for time-of-flight measurements. Figure taken from [31].*

The speed of a particle is given by:

$$v = \frac{L}{t}, \tag{3.1}$$

where:
v= the speed of the particle;
L= the given path length;
t= the time of flight.

The equation 3.1 can be express using $\beta = \frac{v}{c}$ as:

$$\beta = \frac{L}{ct} \tag{3.2}$$

Therefore, the invariant mass can be written as:

$$m_0 = \frac{p}{c}\sqrt{\frac{c^2t^2}{L^2} - 1} \tag{3.3}$$

As it can be seen in equation 3.3, in order to reconstruct the invariant mass m_0, the information about the momentum of the particle is needed.
This can be measured using a magnetic field which causes the particle to curve because of the Lorentz force into a circular orbit and using a tracking detector to measure the radius of this orbit which is proportional to the momentum of the particle.
The momentum can be expressed using the equality between the centripetal force and the Lorentz force as:

$$\frac{mv^2}{R} = qvB \implies p = qBR \tag{3.4}$$

If two particles with different masses i.e. m_1 and m_2 have the same momentum, the time difference after travelling a given path L is:

$$\Delta t = |t_1 - t_2| = \frac{L}{c}\left|\frac{1}{\beta_1} - \frac{1}{\beta_2}\right| = \frac{L}{c}\left|\sqrt{\left(\frac{m_1c}{p}\right)^2 + 1} - \sqrt{\left(\frac{m_2c}{p}\right)^2 + 1}\right| \tag{3.5}$$

For relativistic particles, $\beta \to 1$ it follows that $p >> mc$, then $(\frac{mc}{p})^2 << 1$, using the Taylor expansion and keeping just the first two terms from the Taylor series i.e. $\sqrt{1 + \left(\frac{mc}{p}\right)^2} \approx 1 + \frac{(mc)^2}{2p^2}$ then equation 3.5 can be written as:

$$|t_1 - t_2| \approx \frac{Lc}{2p^2}(m_1^2 - m_2^2) \tag{3.6}$$

Now it can be defined the separation power of a ToF system, $n_{\sigma_{ToF}}$ as:

$$n_{\sigma_{ToF}} = \frac{\Delta t}{\sigma_{ToF}} = \frac{|t_1 - t_2|}{\sigma_{ToF}} = \frac{Lc}{2p^2\sigma_{TOF}}(m_1^2 - m_2^2) \tag{3.7}$$

where:
σ_{TOF}= system time resolution

The system time resolution σ_{TOF} is defined as:

$$\sigma_{TOF} = \sqrt{\sigma_{start}^2 + \sigma_{stop}^2} \tag{3.8}$$

where:
σ_{start} is the time resolution of the start detector;
σ_{stop} is the time resolution of the stop detector.

If we consider that both detectors have the same time resolution $\sigma_{start} \approx \sigma_{stop} = \sigma$ it follows that the time resolution of a single counter can be expressed as:

$$\sigma = \frac{\sigma_{TOF}}{\sqrt{2}} \tag{3.9}$$

According to the equation 3.7 the separation power of a ToF system, $n_{\sigma_{ToF}}$ increases linearly with the path length L and also it increases with decreasing of the system time resolution σ_{TOF}.
Figure 3.3 depicts the time difference between two particles with different masses and the same momentum as a function of the momentum of the particle. It could be seen that for a given path length of 3.7 m and a system time resolution σ_{TOF} of 100 ps, using $n\sigma$ approach, where n=3, π/κ can be separated up to a momentum of 2.5 GeV/c and K/p can be separated up to a momentum of 3.7 GeV/c. For a system time resolution σ_{TOF} of 50 ps, π/κ can be separated up to a momentum of 3.1 GeV/c and K/p can be separated up to a momentum of 5.2 GeV/c [30].

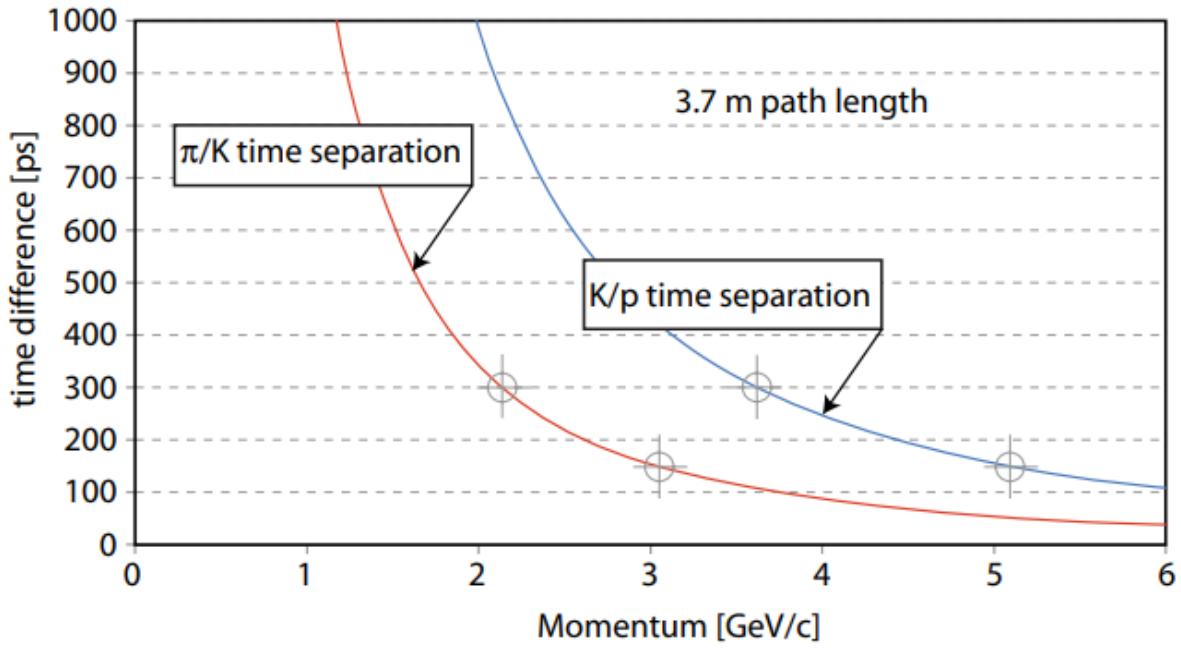

Figure 3.3: *The time difference between 2 particles with the same momentum and different masses as a function of the momentum for 2 different time resolutions of the ToF system i.e.* $\sigma_{ToF} = 100$ *ps and* $\sigma_{ToF} = 50$ *ps, measured over a given path length of 3.7 m. Figure taken from [30].*

The invariant mass can be reconstructed using equation 3.3 and the error associated with the invariant mass can be computed using the error propagation formula.

$$\sigma_m^2 = \left(\frac{\partial m}{\partial p}\right)^2 \sigma_p^2 + \left(\frac{\partial m}{\partial t}\right)^2 \sigma_t^2 + \left(\frac{\partial m}{\partial L}\right)^2 \sigma_L^2 \tag{3.10}$$

It follows that the relative error $\frac{\sigma_m^2}{m^2}$ is:

$$\frac{\sigma_m^2}{m^2} = \frac{\sigma_p^2}{p^2} + \gamma^4 \left(\frac{\sigma_t^2}{t^2} + \frac{\sigma_L^2}{L^2}\right) \tag{3.11}$$

It is worth mentioning that the momentum p can be measured with good accuracy of $\frac{\sigma_p^2}{p^2} \approx 1\%$ and the track length error is below 1 cm i.e. $\frac{\sigma_L^2}{L^2} < 10^{-3}$ [29, 30].

As an example, Figure 3.4 shows a PID spectrum using the time-of-flight method taken with the ALICE ToF detector from p-p collisions at 7 TeV. It shows that using this method charged hadrons can be identified. Bands from the left side are anti-particles because they are deflected to the left due to the magnetic field and particles from the right side have a positive charge and are deflected to the right due to the magnetic field. Also, it can be seen that particles with momentum < 300 MeV/c could not be identified because they do not reach the detector due to their curvature in the magnetic field.

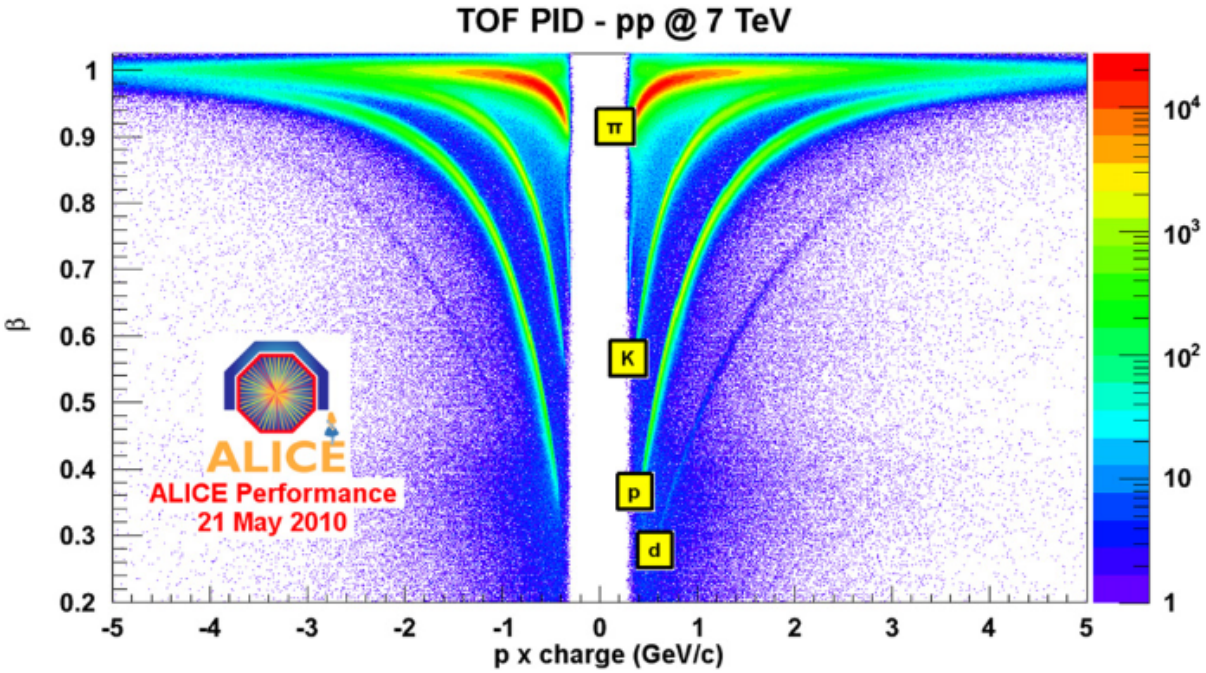

Figure 3.4: *A PID spectrum using the time-of-flight method. Figure taken from [29].*

3.2 The inner wall of the CBM ToF system

The most challenging zone in terms of the counting rate of the ToF wall is the inner zone which will be exposed to counting rates up to 40 kHz/cm^2 in the region of

low polar angles. Radiation hard, high time resolution and two-dimensional position sensitive MSMGRPCs detectors with high granularity are needed in order to maintain the requirements of the CBM-ToF system i.e the efficiency above 95% and a system time resolution better than 80 ps with occupancy below 5% at such a tremendous counting rate. The incident particle flux, as well as the hit density, have a strong dependence on the polar angle, therefore the inner wall is based on three types of MSMGRPCs detectors with different granularities i.e. 56/96/196 mm (strip length) × 300 mm. The architecture of the inner zone of the ToF system is presented in Figure 3.5.

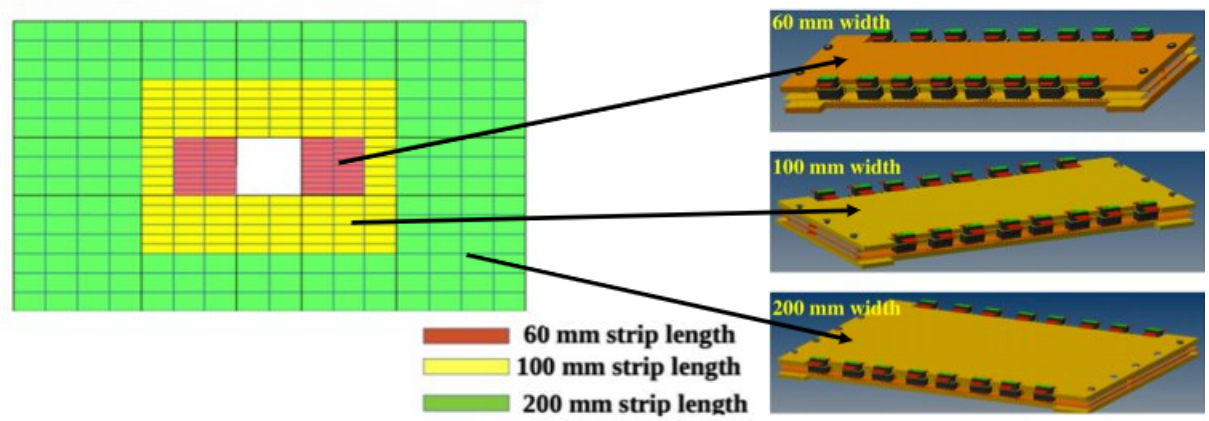

Figure 3.5: *The architecture of the inner zone of the CBM ToF system based on 3 types of MSMGRPCs with different granularities.*

The active area of the inner zone is about 15 m^2 and it has a modular architecture organized in 12 modules of 4 types. A sketch of the inner zone is depicted in Figure 3.6.

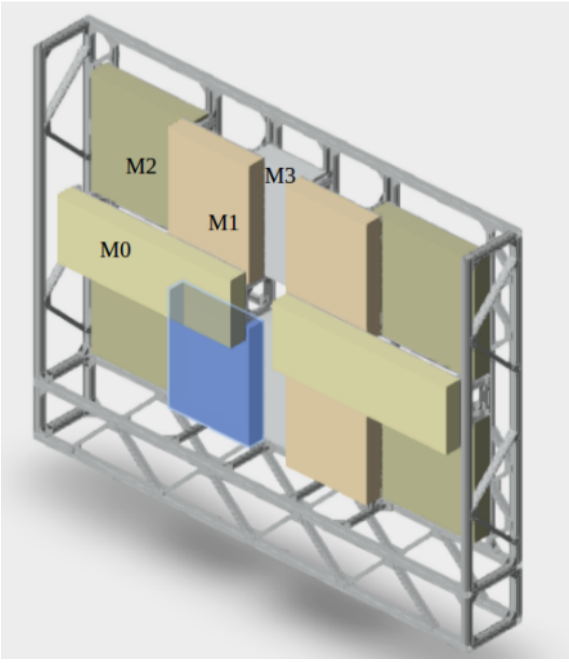

Figure 3.6: *A 3D representation of the inner zone. It can be seen that it has a modular architecture. Figure taken from [32]*

The design of one of the modules of the inner zone, module M0, is presented in Figure 3.7

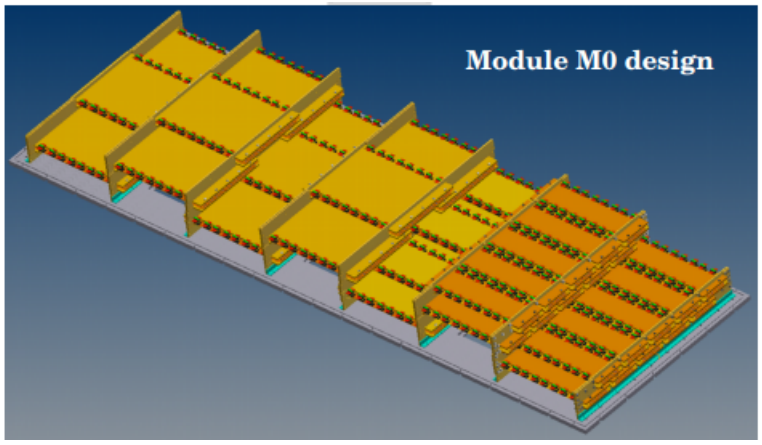

Figure 3.7: *A sketch of a module from the inner zone of the ToF wall i.e. M0 module.*

Chapter 4

Resistive Plate Chambers

Resistive Plate Chambers (RPC) [33] are one of the most used gaseous detectors in large experimental arrangements, especially for high energy physics experiments being used either as trigger detectors or timing detectors due to a very good time resolution at an efficiency over 95% for minimum ionizing particles [34].
Various improvements were done over the years which led to radiation hard, high time resolution and two-dimensional position-sensitive detectors which can cover large experimental areas [35].
As any type of detector, RPC counters suffer from so-called ageing effects because of their operation in high irradiation dose which leads to a deterioration of their performances over time. Using these detectors in large heavy-ion experimental arrangements, especially for the next generation of high interaction rate experiments where free-streaming data acquisition will be based on self-triggered electronics, reducing the ageing effects of the counters are of paramount importance for ensuring the quality of the experimental data. For reducing the ageing effects at maximum, but at the same time maintaining the performance, a new generation of the RPC has been developed.

4.1 The working principle of the RPC detectors

As any type of particle detector, the working principle lies in the interaction of radiation with matter [36]. The incident particles transfer a part or all of their energy to the active medium of the detector through direct or indirect mechanisms generating a recognizable signal.
Being a gaseous detector, the interaction of radiation in the gas medium of the RPC counters leads to a release of electron-ion pairs. Using a planar geometry of the electrodes where a voltage difference is applied in between, which generates a uniform electric field between the parallel plates, the primary ion-electron pairs are accelerated immediately after their generation in a high enough electric field. Therefore, an electron can gain enough energy to induce multiple inelastic processes i.e. excitation and ionization of the gas molecules which will lead to new electron–ion pairs. These processes can be written as:
The excitation process:

$$X + p \longrightarrow X^* + p, \tag{4.1}$$

The ionization process:

$$X + p \longrightarrow X^+ + p + e^- \tag{4.2}$$

where:
X is a gas molecule;
p is an incident particle.

Due to this multiplication process, an avalanche is formed. The electrons drift towards the anode and ions drift towards the cathode due to the electric field. The drift velocity of the electrons in gas is much larger than the drift velocity of ions by a factor of the order of 1000, therefore an avalanche has a drop-like charge distribution which has a head created by the fast electrons and a slow ions trail at the end.
The average distance that an electron has to travel between two consecutive collisions to produce an ionization is called mean free path λ and the number of electron-ion pairs produced by the electron drifting towards anode per unit length α is called the first Townsend coefficient and it can be written as:

$$\alpha = \frac{1}{\lambda} \tag{4.3}$$

Figure 4.1 shows the first Townsend coefficient α as a function of the applied electric field for a typical gas. It can be seen that α is 0 for the electric below a certain threshold which is the threshold for the gas multiplication and above the threshold it is a function of the electric field strength. The threshold is around 10 kV/cm [37].

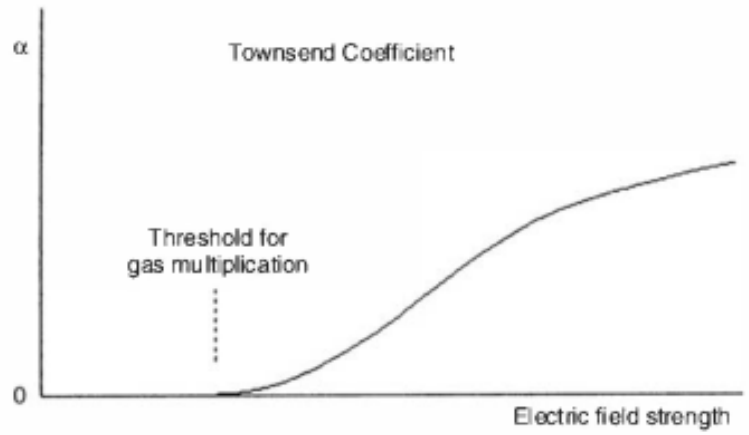

Figure 4.1: *The first Townsend coefficient as a function of the electric field strength. Figure taken from [37].*

If it is considered an initial number of n_0 electrons in a given position from the counter, the infinitesimal increase of the number of free electrons dn, due to the multiplication process after a path length dx is:

$$dn = n_0 \alpha dx \tag{4.4}$$

For a parallel plate geometry where the electric field is uniform, α is a constant in the Townsend equation i.e. 4.9. Therefore, integrating over the path length x:

$$n = n_0 e^{\alpha x} \tag{4.5}$$

The multiplication factor also called the gas gain can be written as:

$$M = \frac{n}{n_0} = e^{\alpha x} \tag{4.6}$$

Excited molecules and atoms of the gas can de-excite by various processes i.e. radiative channels by emission of UV photons and by non-radiative processes. The UV photons can generate electron-ion pairs in the electric field, hence the photoelectron can trigger a secondary avalanche. If the probability of an electron from the primary avalanche to producing a photoelectron is γ_{photo}, then the total number of photoelectrons produced in an avalanche can be written as:

$$n_{photoelectrons} = M n_0 \gamma_{photo} \tag{4.7}$$

If the applied electric field is very high, a transition from the avalanche to streamer may occur which can be thought of as a thin plasma channel. This could happen when $n_0 M > 10^8$ electrons which is called Reather's limit.
In order to avoid corona discharge which can occur when $\mathrm{M}\gamma_{foto} \longrightarrow 1$ i.e. each primary electron generates a secondary avalanche, a gas mixture with quenching properties i.e. a gas which has a high absorption UV coefficient and it can de-excite through a non-radiative channel together with a small amount of an electronegative gas in order to capture the free electrons which can trigger secondary avalanches can be used. Therefore, the attachment processes that occur in such a gas mixture have to be taken into account at computing of the gas gain.
The attachment coefficient η can be defined as the probability for an electron to undergo an attachment process per unit length. Therefore, the Townsend equation i.e. 4.9 can be rewritten as:

$$dn = n_0 \alpha^* dx \tag{4.8}$$

where
$\alpha^* = \alpha - \eta$ is called the effective first Townsend coefficient.

For a uniform electric field, integrating over the path length x, the total number of electrons generated in an avalanche is:

$$n = n_0 e^{\alpha^* x} \tag{4.9}$$

And the multiplication factor or the gas gain can be written as:

$$M = \frac{n}{n_0} = e^{\alpha^* x} \tag{4.10}$$

The formation of an avalanche and its dynamics is depicted in Figure 4.2. A free electron drifts in the electric field and undergoes multiple inelastic processes due to electromagnetic interaction with the Coulomb field of the gas molecules which leads to excitation and ionization of the atoms and molecules of the gas, generating electron-ion pairs, but also it undergoes elastic collisions which lead to a change in its trajectory without losing its kinetic energy.

The RPC detectors use resistive electrodes with a resistivity in the order of $(10^8 - 10^{12}\ \Omega \cdot cm)$ for self-quenching, hence when an avalanche or a streamer reaches the surface of a charged resistive electrode, takes place a localized discharge of the electrode which leads to a localized dead zone of a few hundred of μm, but the rest of the detector remain

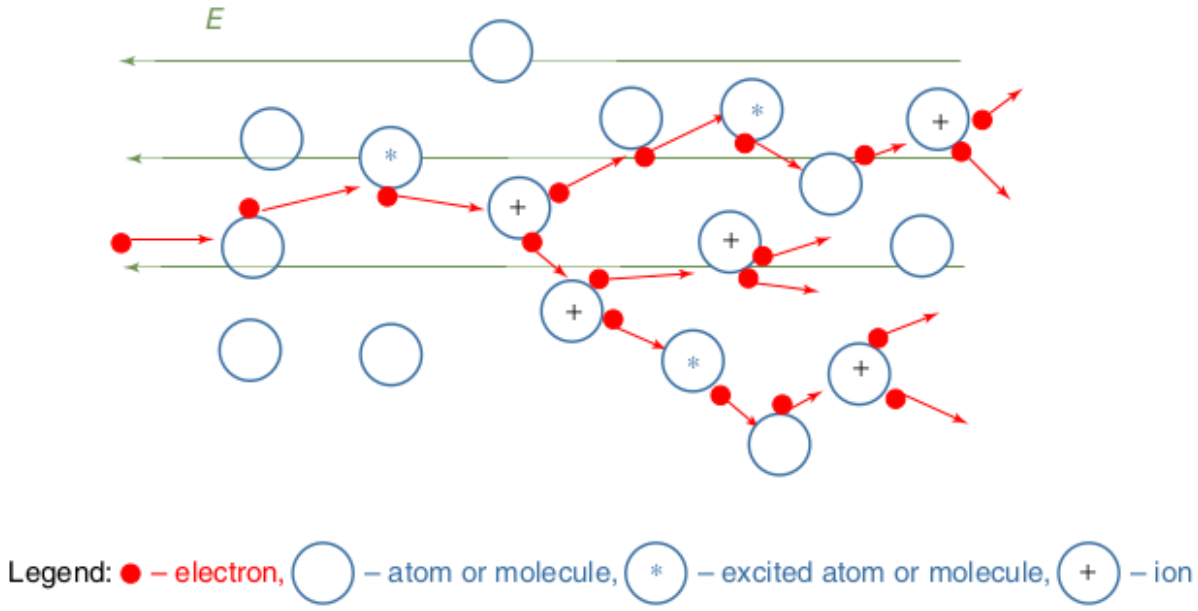

Figure 4.2: *The dynamics of an avalanche. Figure taken from [33].*

fully sensitive and it can detect another particle.
The time constant τ of the detector represents the time interval needed for the localized discharge to recharge and it is defined as:

$$\tau = RC = \rho\epsilon_0\epsilon_r \tag{4.11}$$

where:
R= $\frac{\rho d}{A}$ is the resistance of the electrodes;
C= $\epsilon_0\epsilon_r\frac{A}{d}$ is the capacitance electrode plates;
ρ is the resistivity;
$\epsilon_0 \approx 8.854 \cdot 10^{-12} F \cdot m^{-1}$ is the vacuum permittivity;
ϵ_r is the relative permittivity of the resistive plate;
A is the surface of the plate;
d is the thickness of the plate.
As it could be seen in equation 4.11 one way in which the dead time for the discharged spot can be reduced is to use low resistivity electrodes which can increase the rate capability of the RPC allowing it to be used in high counting rate experiments.

4.2 The evolution of parallel plate gaseous detectors

4.2.1 Parallel Plate Counters (PPC)

In 1948 J.W. Keuffel had for the first time the idea of using a parallel plate geometry for a gaseous detector. The advantage of using this geometry is that the electric field is uniform in the whole active area of the counter. Therefore, an electron-ion pair is produced by the incident particle inside the amplification region where it will trigger an avalanche and if it reaches the Reather's limit, then it will transform into a streamer.

When the streamer reaches the metallic electrodes a spark occurs. Because of this fast response time, Parallel Plate Counter has a very good time resolution in the order of tens of ns and an efficiency over 90% in cosmic ray tests. PPC has metallic electrodes and is operated in spark mode. After an ionizing particle crosses the counter, continuous discharges take place, therefore a constant high voltage could not be used and a pulsed or triggered operation mode was developed. Because of the use of a pulsed high voltage, the dead time of the counter was very high and the rate capability was very low. Furthermore, the lifetime of the counter is limited to a few months because of its operation in spark mode.

4.2.2 Parallel Plate Avalanche Counters (PPAC)

In order to increase the rate capability and the lifetime of the PPC a new type of counter was developed. Parallel Plate Avalanche Counter (PPAC) [38] is not operated in spark mode anymore but rather in avalanche mode. It also has metallic electrodes but by applying a lower voltage, the avalanche does not reach Reather's limit. This fact allows these counters to be operated with a constant high voltage and they have a better time resolution, below 1 ns. Because these counters are operated in avalanche mode, the signals are lower and a dedicated front-end electronics was developed. PPAC has metallic electrodes and it has a tendency towards corona discharges and the sparks can damage both the detector itself and the front-end electronics.

4.2.3 Pestov Counter

In 1971 Yu. Pestov developed a new type of counter with a parallel plate geometry using a resistive plate i.e. the anode which was made from a special semi-conductive glass doped with Fe^+ with a resistivity in the order of $5 \cdot 10^9\ \Omega \cdot cm$ also known as Pestov glass and the cathode was made from copper [39]. The idea of using a resistive glass plate was a true breakthrough because opened a new area for the parallel plate gaseous detectors. The counter was operated in spark mode, but due to the resistive electrode, the high voltage drops only around a small area where the discharge takes place, hence the dead area is about 1 mm^2 and the rest of the counter remains sensitive to other particles. This self-quenching mechanism allowed building bigger counters up to a few hundred square centimetres. The gas mixture was based on Ar/Ne and some organic gases for quenching i.e. absorption of UV photons of different energies and the gas pressure was 12 bars. The gas gap was 100 μm and reached an efficiency over 96% and a time resolution of 25 ps. Pestov counters were based on strip readout, therefore they are two-dimensional sensitive, having a spatial resolution along the strip of 2.5 cm and across the strip of 300 μm. Because of the observed tails in the time distribution beyond the Gaussian curve which have an impact on the data quality of measurements, the high pressure needed for the operation of the counter which implies the use of a special pressure vessel and the fabrication difficulties of the Pestov glass, this type of counter was not used in large experimental arrangements like ALICE or FOPI. However, it was extensively studied by the GSI-FOPI group and they managed to make some correlation between the presence of the tails in the time distribution pointing out that the timing tails depend strongly of the gas mixture i.e. they increase as a function of the noble gas weight, therefore a gas mixture based on Ar is the best choice for reduction of the timing tails and also was

demonstrated that the timing tails are a function of the applied high voltage i.e. they decrease with increasing of the applied high voltage. A sketch of the Pestov counter is depicted in Figure 4.3.

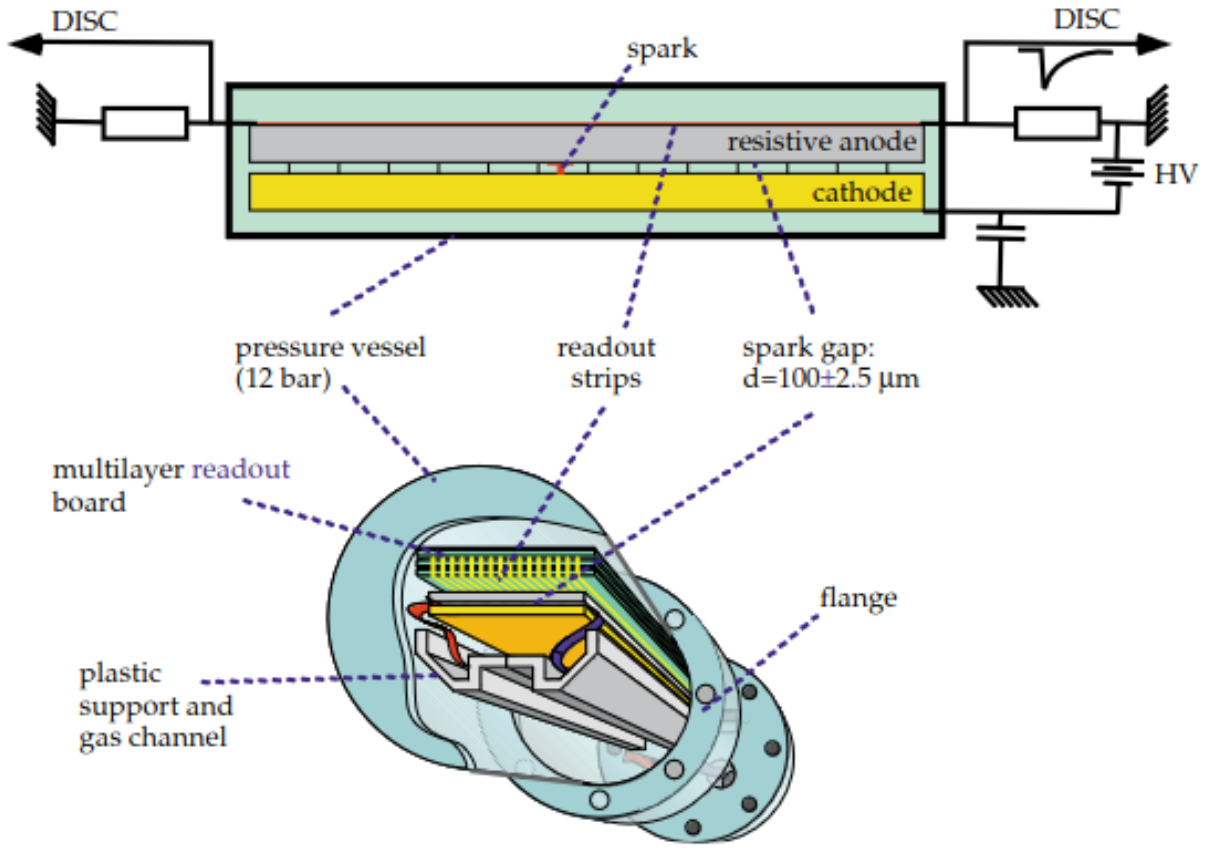

Figure 4.3: *A sketch of the Pestov counter. Figure taken from [39].*

4.2.4 Resistive Plate Chamber (RPC)

In 1981, Rinaldo Santonico and Roberto Cardarelli in Rome, Italy, developed the very first RPC prototype which has both electrodes made from a resistive material i.e. Bakelite which has a resistivity of $10^{10} - 10^{12}\ \Omega \cdot cm$ and was operated at atmospheric pressure in streamer mode. They used 2 mm thick Bakelite electrodes and the gas gap was 2 mm obtaining an efficiency over 95% and a time resolution of 1 ns. Because it was operated in streamer mode, the signals developed were high enough (the integrated charge is in the order of 100 pC) to be read out only by a discriminator and there was no need for using a preamplifier. There was no limitation on the size of the RPC, therefore large area could be covered with this type of detector making it suitable for large experimental arrangements. However, using this counter in heavy-ion collision experiments requires a higher rate capability of this counter, to maintain the efficiency over 95% at a high counting rate and also a better time resolution.

4.2.5 Double gap RPC

In order to obtain a better time resolution at an efficiency of at least 95% and also to increase the rate capability of the counter, Paulo Fonte had the idea of using a double gap architecture of the counter. Because the time resolution is proportional to the gas gap width, a 4×4 cm^2 double gap detector was built with just 300 μm gas gap which had a time resolution of 100 ps. Also, it was tested at counting rates of up to 10 kHz/cm^2 and it had an efficiency over 95% at the working voltage. The physics principle behind a double gap architecture is that an incident particle will create simultaneously, independent avalanches in both gas gaps with a very high probability and the signal induced is the sum of the avalanches from both gas gaps. It has a central readout electrode i. e. the anode such that the electrons produced in both gas gaps drift towards the central anode. Another advantage of using this architecture is the fact that even if the signal from a gas gap is not high enough to pass the front-end electronics threshold, the total amplitude of the signal can pass the front-end electronics threshold and the particle is detected. This technology of RPC is used in large experimental arrangements like CMS (Compact Muon Solenoid) at LHC, at CERN where it is operated in avalanche mode. The parallel plates are made from Bakelite and it has a time resolution of 1.5 ns being used in the muon trigger system. A sketch of this type of RPC is depicted in Figure 4.4.

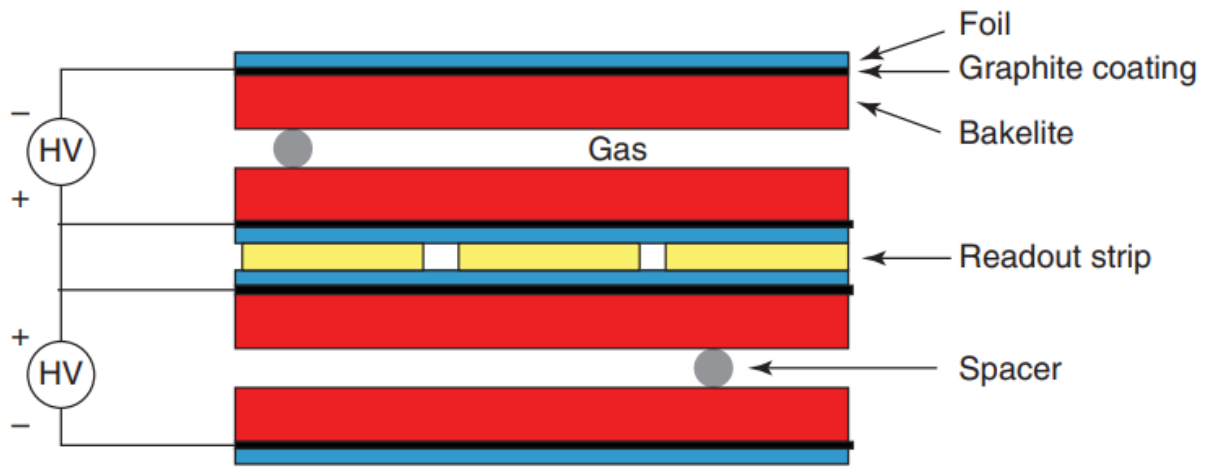

Figure 4.4: *A sketch of a double gap RPC. Figure taken from [33].*

4.2.6 Multi-gap RPC (MRPC)

In order to use RPC detectors for time-of-flight measurements in large arrangements for heavy ion experiments, a time resolution in the order of ps has to be achieved but maintaining efficiency over 95% even at high counting rates. Therefore, in 1996 M.C.S. Williams et al. developed a new type of RPC called Multi-gap RPC [40] for time-of-flight measurements [41, 39]. The electrodes were made from float glass with a resistivity of $10^{12}\ \Omega \cdot cm$. This type of counter was used in time of flight measurements at large experiments, for example, ALICE-ToF, where it was based on two stacks of 5 equally spaced gas gaps of 250 μm and reached a time resolution of about 50 ps at an efficiency over 95%. It is worth mentioning that the statistical fluctuations of the avalanche are very small in narrow-gap RPC.

The high voltage is applied just on the external electrodes and the internal plates are electrically floating. Even though the intermediate plates are not electrically connected, they are at the correct voltage due to the electrostatic effect and are kept at the correct voltage by a feedback mechanism i.e. the flow of electrons and ions restores the electric field even if there is an imbalance in the electric field. The resistive parallel plates are transparent to the induced signal on the external pickup electrodes generated by the moving charge in gaps. When a particle crosses the counter produces independent avalanches in each gas gap with a high probability and the total signal will be the sum of each signal, even more than that if the total signal from a gas gap is not high enough to pass the front-end electronics threshold, the total amplitude of the signal can pass the front-end electronics threshold and the particle is detected. The charge spectrum of an MRPC is a Γ function. Figure 4.5 shows a sketch of an MRPC.

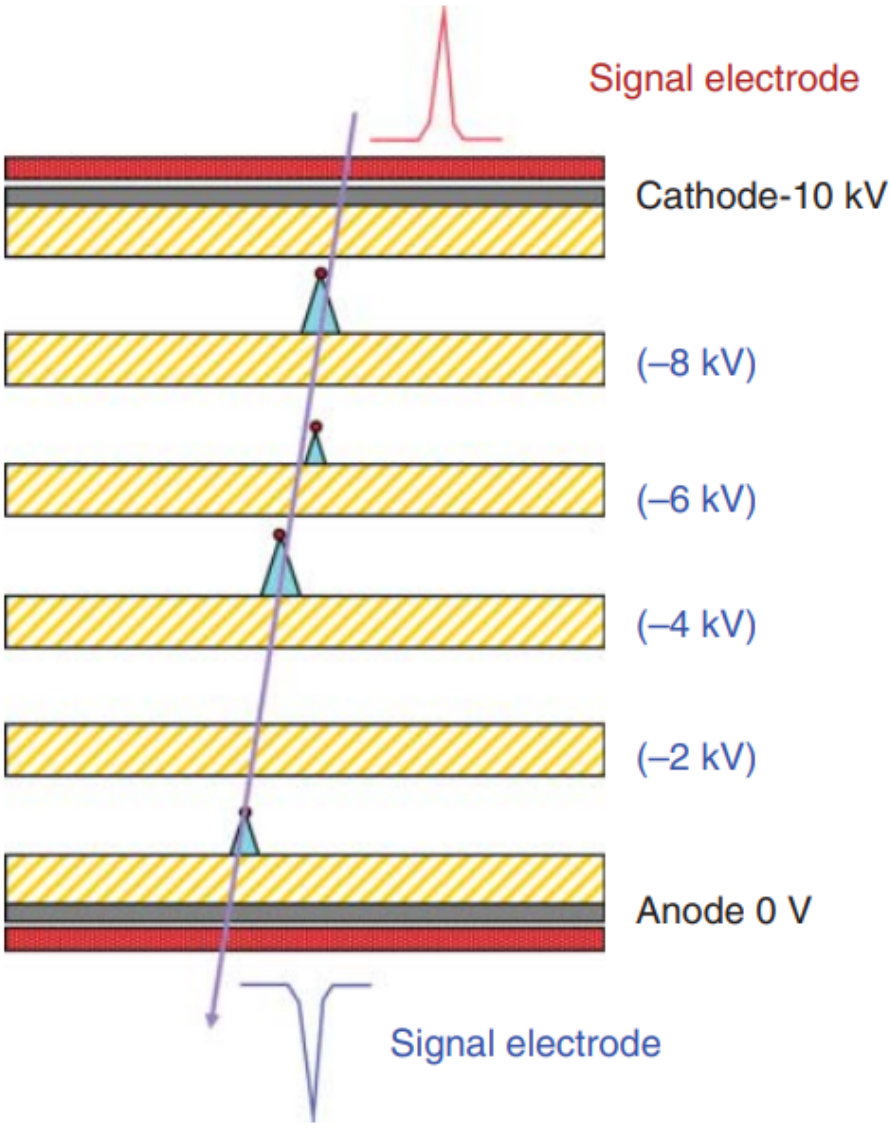

Figure 4.5: *Schematic architecture of the Multi-gap RPC. Figure taken from [33].*

When an ionizing charged particle passes through the gas gap around 5.5 clusters/mm are produced on average. It is worth mentioning that this is a statistical process governed

by the laws of quantum mechanics. Therefore, the probability P for an ionizing particle to produce k clusters in the gas gap can be computed using Poisson's distribution as follows:

$$P(n = k) = \frac{(\lambda_{ef})^k}{k!} e^{-g\lambda_{ef}}, \tag{4.12}$$

where:
$\lambda_{ef} = \frac{\lambda}{cos\phi}$, $0 \leq \phi < \frac{\pi}{2}$;
λ is the average primary cluster density;
ϕ is the azimuthal angle of the incident particle;
g is the gas gap width.

The average value of this distribution is $g\lambda_{ef}$.
The intrinsic inefficiency of the counter is defined as the probability that an incident particle which crosses the counter will not produce any cluster i.e. no avalanche in a gas gap, therefore it will not undergo an interaction in that gas gap. It can be computed as follows:

$$P(n = 0) = e^{-g\lambda_{ef}} \tag{4.13}$$

For a gas gap of 200 μm the intrinsic inefficiency is about 11% which represents the probability that an incident charged particle that crosses the counter will not produce an avalanche in that gap.

4.3 High time resolution, two dimensional-position sensitive Multi-Strip Multi-Gap Resistive Plate Counter (MSMGRPC)

Time-of-flight measurements of the products from collisions require detectors with a time resolution better than 100 ps, but also large arrangements have to be covered with such detectors. MRPC are the most suitable choice because of their performance in terms of very high efficiency and excellent time resolution. However, MRPC is read out by pad electrodes which do not offer bidimensional position resolution. Therefore, in 2002 Petrovici et al. proposed a completely new detector concept [35], MSMGRPC which is read out via multistrip anodes. Using readout strips, position information along and across the strip can be achieved [34]. The position information along the strip is calculated using the time difference between the left and right side of the strip i.e. $y = (t_l - t_r) \cdot v/2$, where v is the signal velocity, and position information across the strip can be computed using the well-known centre of gravity method. Therefore, this new detector concept of MRPC readout by strips electrodes, called Multi-Strip Multi-Gap Resistive Plate Counter (MSMGRPC) which has a very good time resolution and offers position information in two dimensions is the best choice for the time of flight measurements for high energy physics experiments [42].
For the first time, MSMGRPC based on float glass was used at the FOPI experiment, for the upgrade program for the time-of-flight barrel [43], where 150 MSMGRPCs with 8 gas gaps of 220 μm, covering an active area 5 m^2, cylindrical arranged, formed a time of flight barrel with an extended PID capacity to identify kaons up to a momentum of

$p_{lab} \approx 1$ GeV/c. The time resolution of the MSMGRPC was around 60 ps and the position resolution along the strip was σ_z=1.5 cm and across the strip was σ_z=1.7 mm and the efficiency was $\epsilon > 99\%$.

4.3.1 The MSMGRPC for the inner zone of the Time-of-Flight system of the CBM experiment

At the CBM experiment which is designed to run at very high interaction rates of up to 10 MHz for Au-Au collisions, at 8 m from the target, at the low polar angles covered by the experiment, high particle densities with rates of up to $4 \cdot 10^4$ Hz/cm^2 are expected. The requirements for the detectors of the ToF system are a time resolution better than 80 ps and an efficiency over 95%, maintaining these performances at a high counting rate in order to perform a very good PID.
In order to fulfil these requirements, a MSMGRPC based on low-resistivity glass electrodes ($\rho \approx 1.5 \cdot 10^{10}$ $\Omega \cdot cm$) [44] was built [45].
It consists of 2 identical symmetric halves of the multi-gap RPC detector architecture relative to the central multi-strip anode electrode. Each stack has 6 low resistivity glass plates of 0.7 mm thickness, 300 mm length and 60 mm width which corresponds to the highest granularity detector from the inner zone of the ToF system. They are equally spaced by a nylon fishing line and form 5 gas gaps of 200 μm. The high voltage is applied using electrodes based on Cu strips of 9.02 mm strip pitch and 7.37 mm strip width which are in tight contact with the outermost glass plates of each stack. The readout electrodes are designed with 32 strips of 9.02 mm strip pitch and 1.27 mm strip width which have an impedance of 97 Ω matched to the front-end electronics impedance for the given granularity of the counter. A sketch of MSMGRPC detector is depicted in Figure 4.6.

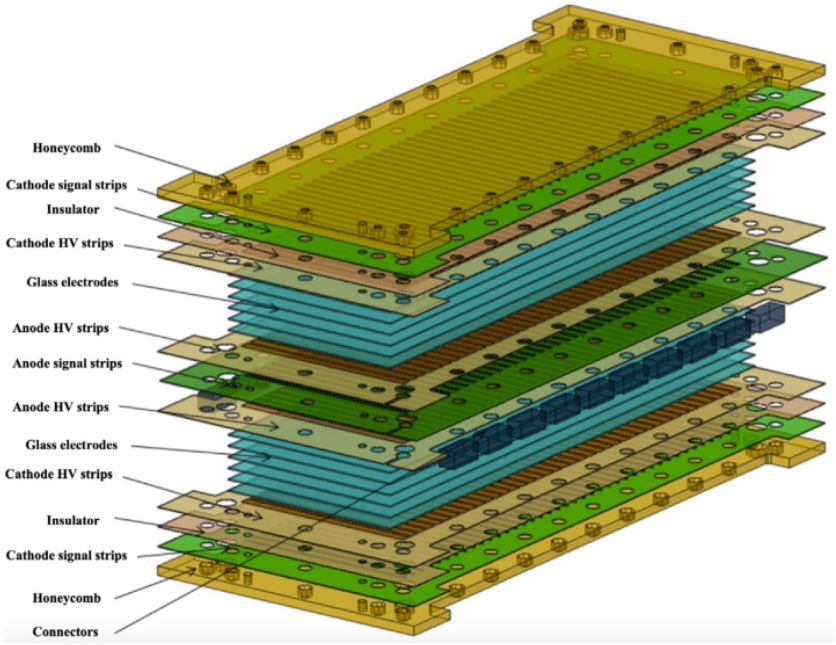

Figure 4.6: *A sketch of the MSMGRPC. It has 2 identical symmetric halves of the multi-gap RPC detector architecture relative to the central anode electrode. Figure taken from [45].*

The granularity of the counter is determined by the HV strip length and the cluster size and the impedance of the transmission line is determined by the pick-up strip width and the electric properties of the structure in between. In order to match the impedance of the transmission line of the counter to the impedance of the front-end electronics for a given granularity of the counter a new method was developed which implies a different ratio of the HV and pick-up strip widths for the same strip pitch [46]. This matching is extremely important, especially for a free-running mode experiment in order to avoid reflections.
Figure 4.7 shows the pick-up multi-strips anode electrode overlapped on the HV strips electrode.

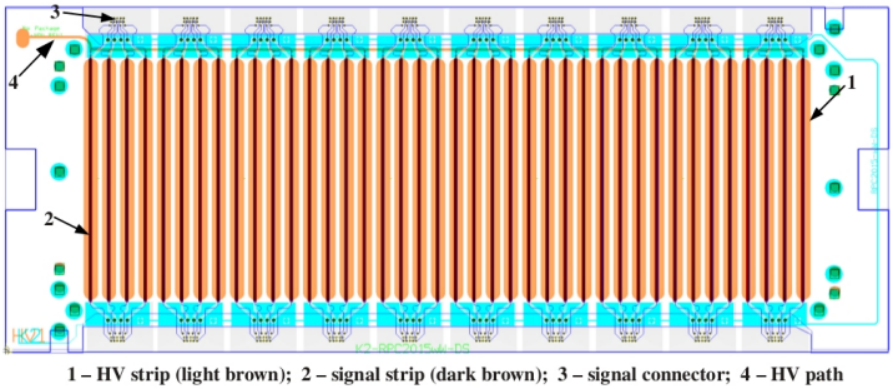

Figure 4.7: *The high voltage electrode overlapped over the anode readout electrode. It can be seen a different ratio of the HV and pick-up strip widths for the same strip pitch. Figure taken from [45].*

The signals of the counter are read out in a differential mode which means that both positive and negative signals are recorded. Figure 4.8 depicts positive and negative signals recorded using an oscilloscope. It can be seen that there are no reflections on the oscilloscope time scale i.e. 25 ns which means a very good matching between the impedance of the transmission line and the impedance of the front-end electronics.

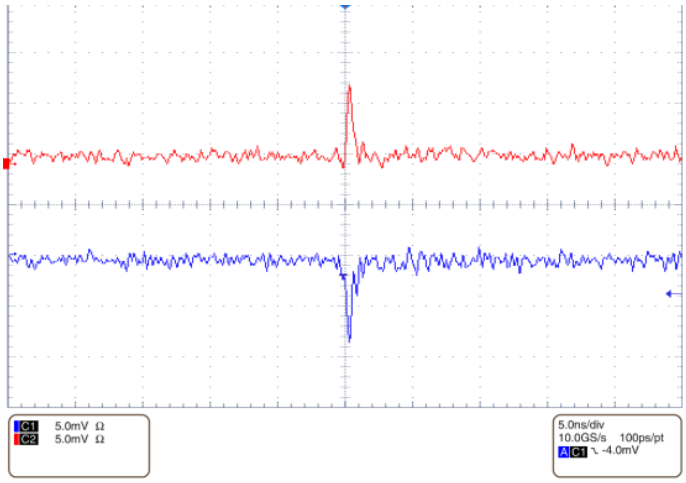

Figure 4.8: *Positive (red) and negative (blue) signals of MSMGRPC recorded using an oscilloscope. Figure taken from [45].*

Using a gas mixture of 90% $C_2H_2F_4$ (Freon), 5% SF_6 and 5% $i-C_4H_{10}$ cosmic ray tests were performed. An efficiency over 95% at the working voltage $2 \times \pm 5.9$ kV and a time resolution of 67 ps was obtained. It is worth mentioning that the dark current was below 1 nA and the dark counting rate was $\approx$ 1–2 Hz/cm^2 at the working voltage. Therefore, MSMGRPCs fulfil the requirements in terms of efficiency and time resolution for the low polar angles of the inner zone of the CBM-ToF system.

4.4 Ageing studies of MSMGRPC

Produced particles expected for the CBM experiment which will run at interaction rates of up to 10 MHz for Au–Au collisions at $\sqrt{s_{NN}}$= 2-5 GeV are kinematically focused in the forward direction, therefore at 8 m from the target, at low polar angles of the inner zone of the ToF system, detectors have to cope with a very high counting rate of charged particles of up to $4 \cdot 10^4/cm^2 \cdot s$ without deteriorating their performance in terms of efficiency and time resolution over the whole lifetime of the experiment in order to identify with a good accuracy charged particles produced in the collisions.

In order to estimate both ionising and non-ionising dose accumulated, simulations of a beam which has an intensity of 10^9 ions Au/s on a fixed Au target with a probability of interaction of 1% using a Monte Carlo generator i.e. UrQMD (Ultra relativistic Quantum Molecular Dynamics), FLUKA and GEANT3 transport codes were performed [47]. Over a period of 2 months, an ionising dose of $\approx$ 500 Gy and a non-ionising dose of $3 \cdot 10^{11} n_{eq}/cm^2$ are accumulated. The CBM experiment is foreseen to run for 2 months a year for 10 years, therefore ageing tests in high irradiation dose were performed [48] to study the effect of the high-density avalanches over MSMGRPC and find new ways to reduce the observed effects.

MSMGRPC was mounted in a housing box of $\approx$ 13.5l and a gas mixture of 90% $C_2H_2F_4$, 5% SF_6 and 5% $i-C_4H_{10}$ filled the housing box, hence the gas exchange between parallel plates of the MSMGRPC is done by the diffusion process. The spacers used for defining the gas gap of 200 μm were positioned along the strips at a distance of about 35 mm distance one to the other in order to enhance the gas exchange between parallel plates. The counter was exposed to highly energetic photons from a ^{60}Co source with an activity of 360 kCi. The accumulated dose was 12.99 kGy in 10 days, the counter being irradiated for 3 hours a day on average. The accumulated charge was 0.127 C/cm^2. The accumulated charge for the inner zone of the CBM-ToF for a month of data taking for Au-Au collisions at 10 MHz is about 0.72 C/cm^2 per month. After a day after the exposure, it was measured the dark counting rate which was around 20 Hz/cm^2 and the dark current which had a value of 1.27 nA/cm^2. It was observed a recovery process i.e. the dark current and dark counting rate decrease in time and the counter came back to the initial performance. It was pointed out that the dark counting rate is generated in the area around the spacers. The efficiency and the resistivity of the glass plates of the counter had not changed after the irradiation. Also, it was observed depositions on both surfaces of the glass plates. One surface has a high content of fluorine radicals which can produce ablation/etching of the glass surface and the other surface of the glass plate has metallic oxide depositions.

Chapter 5

An innovative architecture of MSMGRPCs for the inner zone of the CBM-ToF system

In order to reduce the observed ageing effects induced by the high-density avalanches due to high irradiation dose and the gas pollution effects observed in the MSMGRPC [48], a completely new counter architecture was developed. Based on studies from low-pressure plasma where it was evidenced that the polymerisation process is inversely proportional to the gas flow [49], an innovative architecture of the counter with a directed gas flow through the gas gaps was designed. A new prototype was assembled and tested [50].
Ageing studies previously performed [48] showed a higher dark counting rate and also higher depositions in the spacer region because of slower gas exchange. In this new architecture of the counter, 2 spacers were positioned outside of the electric field, running across the strips at 1 mm apart from the glass edge. However, due to the electric force which causes parallel plates to bend, reducing the gas gap which leads to corona discharges, the minimum distance between 2 consecutive spacers has to be around 30 mm which made necessary another spacer to be placed in the electric field for 56 mm strip length counter. For the 96 mm strip length counter, 2 spacers were necessary to be placed in the electric field and for the 196 mm strip length prototype 4 spacers were placed in the electric field to avoid deformation of the parallel plates.
The gas exchange between the gas gaps for the previous architecture of MSMGRPC takes place by a diffusion process which leads to a lower gas exchange rate than the new architecture of MSMGRPC where the working gas is directed through the gas gaps. The gas mixture will be based only on 97.5% $C_2H_2F_4$ (Freon) and 2.5% SF_6. In order to reduce the content of fluorine radicals a lower concentration of 2.5% SF_6 will be used.
Figure 5.1 depicts the structure of the 96 mm strip length counter where it can be seen 2 nylon fishing line spacers placed in the electric field and 2 spacers placed outside the electric field.

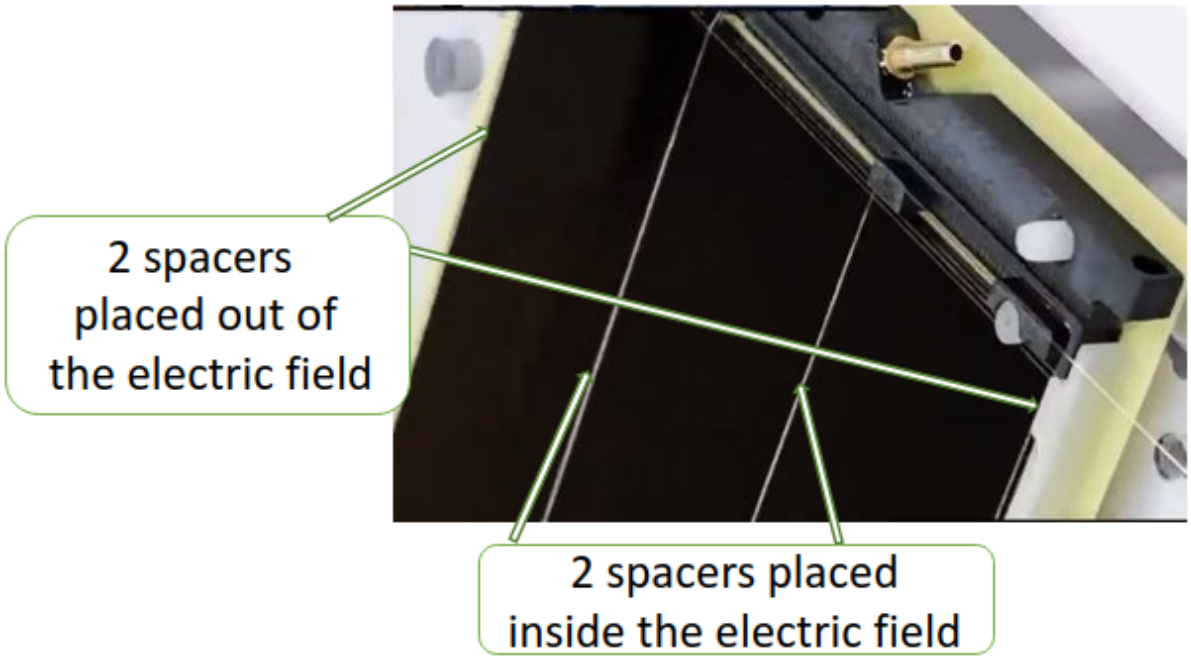

Figure 5.1: *A photo of the structure of MSMGRPC. 2 spacers distributed along the resistive plate out of the electric field and 2 spacers placed inside of the electric field.*

Figure 5.2 shows a sketch of the structure of the new architecture of MSMGRPC. The gas fills the counter through the gas guides and using 2 epoxy glass fiber ledges makes a frame sealed by a silicon paste.

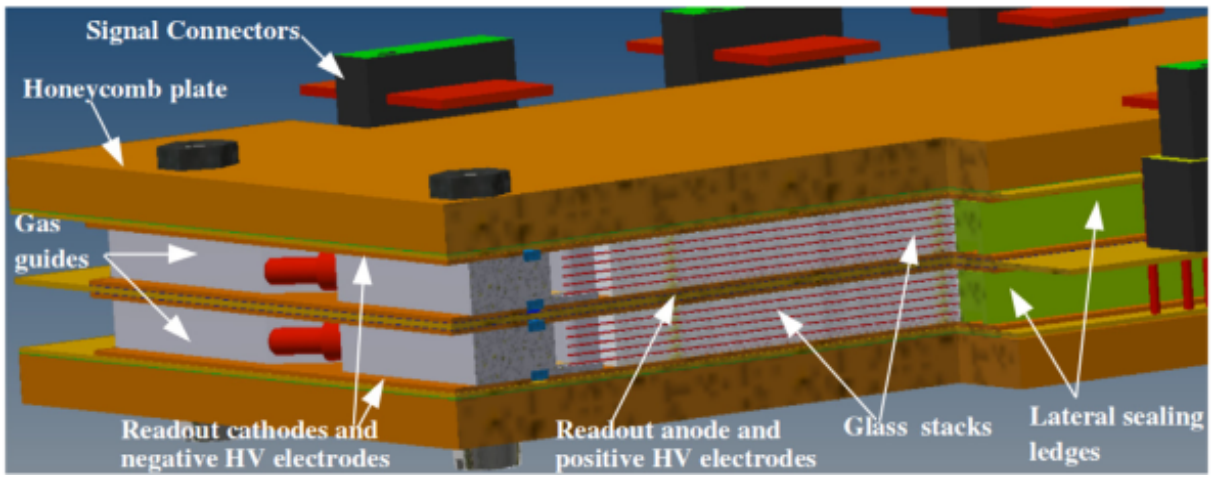

Figure 5.2: *The structure of the MSMGRPC with a direct flow through the gas gaps. Figure taken from [51].*

5.1 The 56 mm strip length MSMGRPC prototype

A prototype with the new architecture which has a 56 mm strip length i.e. the counter with the highest granularity, was assembled. It is depicted in Figure 5.3.

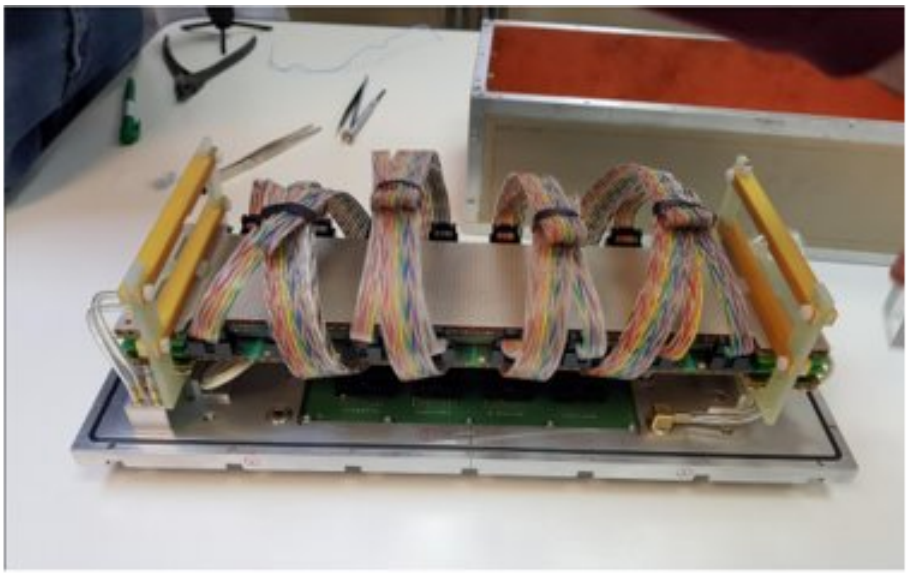

Figure 5.3: *A photo of the direct flow prototype MSMGRPC of 56 mm strip length after assembling.*

Figure 5.4 shows typical signals recorded using an oscilloscope of a ^{60}Co source which has an activity of 1 MBq. Positive signals are taken from the anode and negative signals are taken from the cathode. It can be seen that on the time scale of the oscilloscope i.e. 25 ns there are not reflections meaning that there is a very good impedance matching.

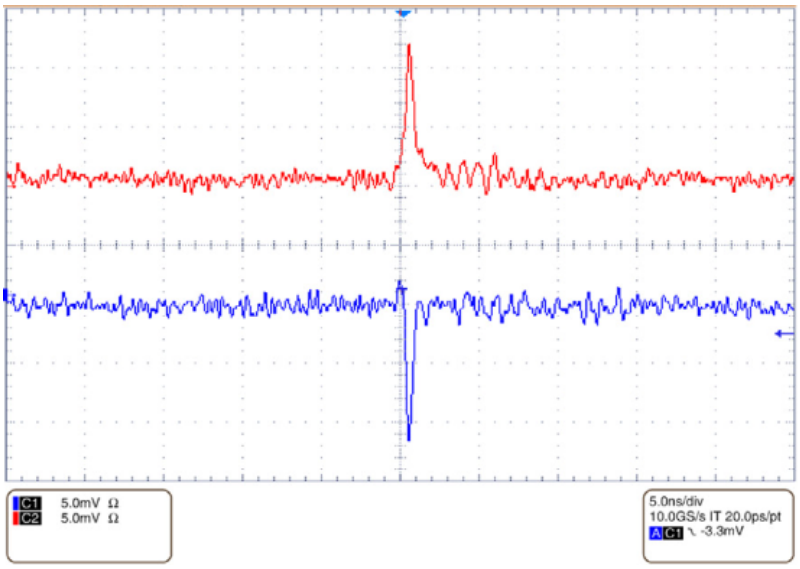

Figure 5.4: *Positive (red) and negative (blue) signals of the direct flow MSMGRPC prototype recorded using an oscilloscope. Figure taken from [51].*

The counter was tested in-beam at mCBM experimental setup [52] at SIS 18 accelerator, in high counting rate runs [50]. Produced particles from a ^{16}O beam with an energy of 2 A $\cdot$ GeV on a fixed target of Ni were used to test the counter.
At the working voltage, the time resolution of the counter was 52 ± 0.7 ps, measured at a counting rate of 1 kHz/cm^2. No degradation of the time resolution of the counter was

observed up to the highest counting rate i.e. 20 kHz/cm^2.
Figure 5.5 shows the time difference between the mean times, $(t_l + t_r)/2$, of correlated hits within a time window and a position window between MSMGRPC and a reference detector. The time resolution is equal to the standard deviation σ of the Gaussian fit of the time spectrum divided by $\sqrt{2}$ considering $\sigma_{MSMGRPC} \approx \sigma_{Ref}$. PADI XI [53] was used as amplifier/discriminator and GET4 TDC [16]. Time measurements were corrected for systematic errors i.e. walk correction.

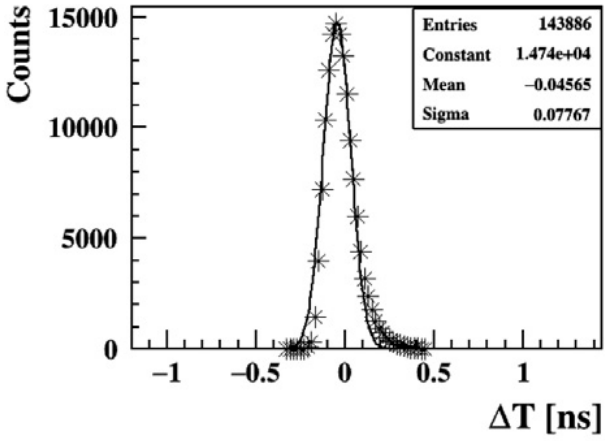

Figure 5.5: *Time spectrum of MSMGRPC fitted with a Gaussian function. Figure taken from [50].*

The rate capability of the MSMGRPCs is showed in Figure 5.6 where at interaction rates of up to 20 kHz/cm^2 it was able to reconstruct the beam spill profile. It is very well known that the spill structure of a synchrotron is not uniform and this was turned out using high rate MSMGRPCs.

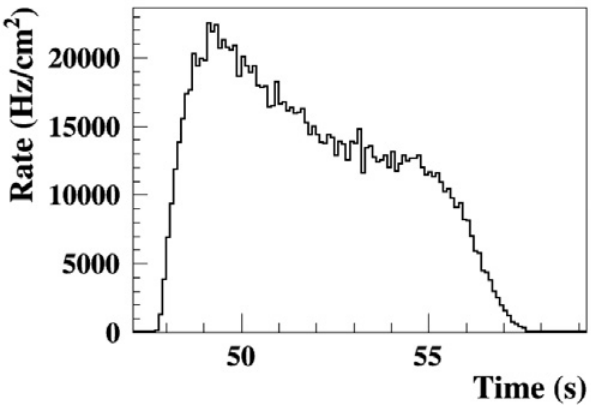

Figure 5.6: *The beam spill structure recorded with high rate MSMGRPC. Figure taken from [50].*

It was proved that the new architecture of MSMGRPC with a directed flow through the gas gaps fulfils the requirements in terms of rate capability and time resolution for the inner zone of the CBM-ToF system.

In order to test the performances of this new architecture in terms of ageing effects, 2 X-ray tubes were used. Also, the previous architecture of MSMGRPC, where gas exchange

takes place via diffusion, which has the same number of gas gaps and the same size of the gas gap as the new architecture of MSMGRPC was exposed to X-rays in order to be taken as reference.
Both counters were equipped with NINO amplifier/discriminator [54]. The threshold of the front-end electronics was set at 145 mV. The strips were read at both ends by the NINO chips after that it was performed a logic AND between the signals from both ends of a strip in order to avoid spurious signals after that a logic OR between the outputs of all logic ANDs was performed. The logic OR signals were recorded using a scaler with a timer.
The distance between the X-ray tubes and the counter was 14 cm such that to ensure uniform exposure of the counter over the whole surface. The experimental arrangement is showed in Figure 5.7.

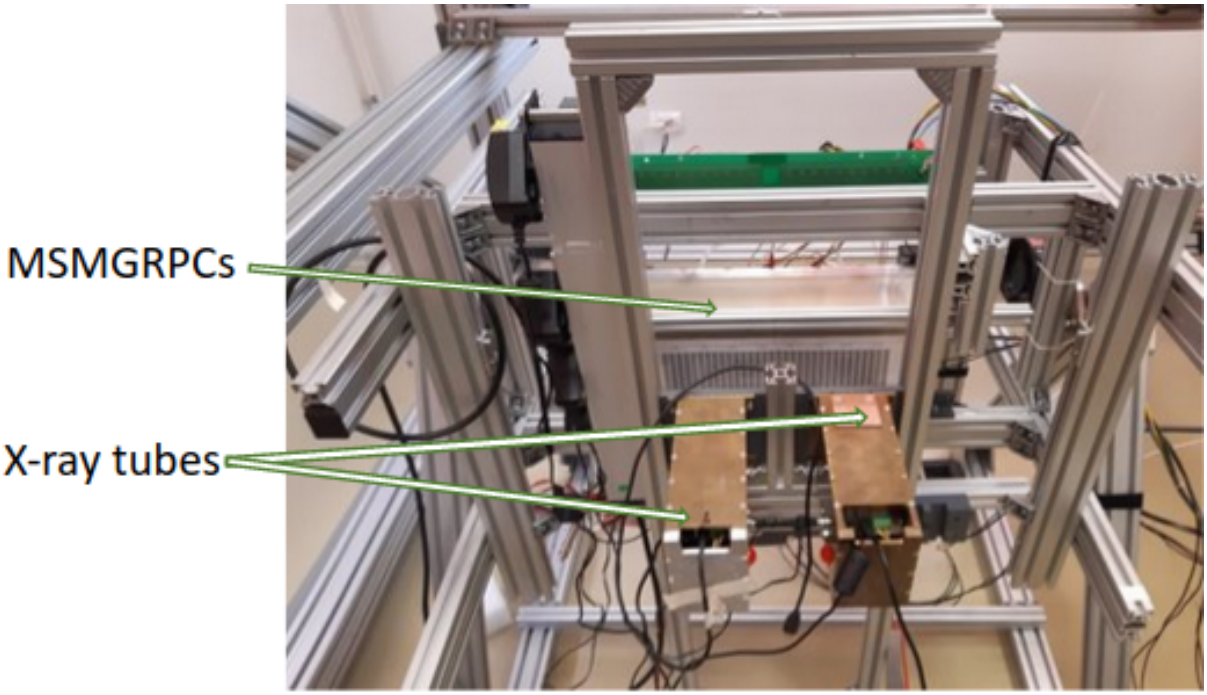

Figure 5.7: *The experimental arrangement for X ray tests.*

First of all, for both counters a calibration curve in terms of current as a function of counting rate up to 28 kHz/cm^2 was performed. The calibration curve obtained with the prototype where the gas exchange takes place via diffusion is showed in Figure 5.8. It was used a flow rate of 4 l/h. It can be seen that the calibration curve has a linear behaviour for a counting rate of up to 15 kHz/cm^2. At higher counting rates a slight deviation from linearity was observed which can be explained by the logic electronic scheme used for estimating the counting rate. The experimental points were fitted using a second-order polynomial function. The calibration curve exhibits a similar behaviour for both counters.

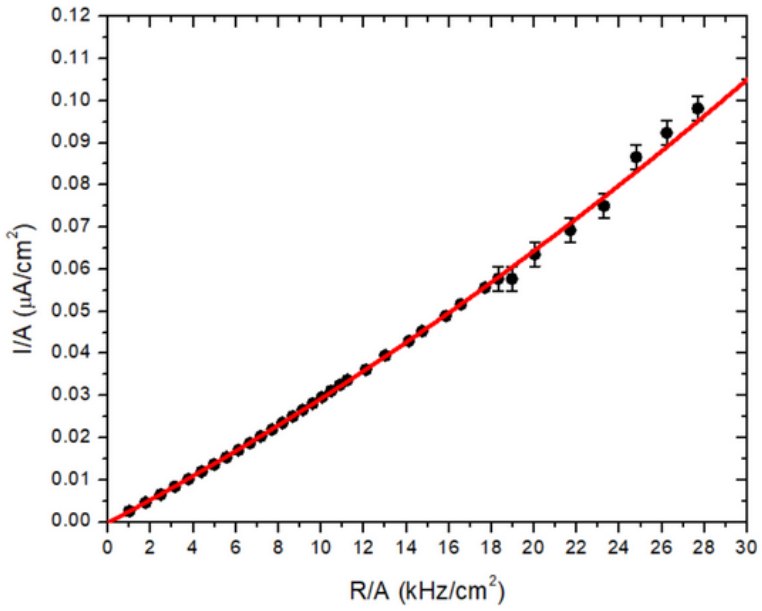

Figure 5.8: *The calibration curve in terms of current as a function of counting rate.*

Figure 5.9 depicts signals taken with the direct flow MSMGRPC prototype using an oscilloscope during the irradiation at the maximum counting rate reached using both X-ray tubes placed at a proper distance from the counter. It can be seen that there is no sign of pile-up effects which shows the high rate capability of MSMGRPC.

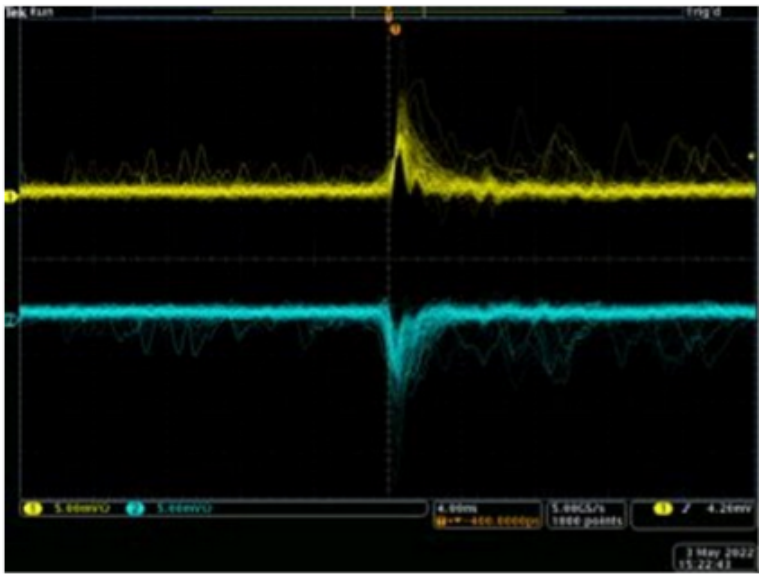

Figure 5.9: *Positive (yellow) and negative (blue) signals of the direct flow MSMGRPC prototype at the highest counting rate recorded using an oscilloscope.*

Both counters were exposed for about 5 hours a day for many days at the highest counting rate reached using both X-ray tubes and the current and counting rate during the exposure were recorded. The gas flow rate was 4 l/h for all exposures for both counters. Figure 5.10 shows the current on the left side and the counting rate on the right side during the exposure for the MSMGRPC prototype where the gas exchange takes place via diffusion. It can be seen that both current and counting rate have a constant value

during exposure.

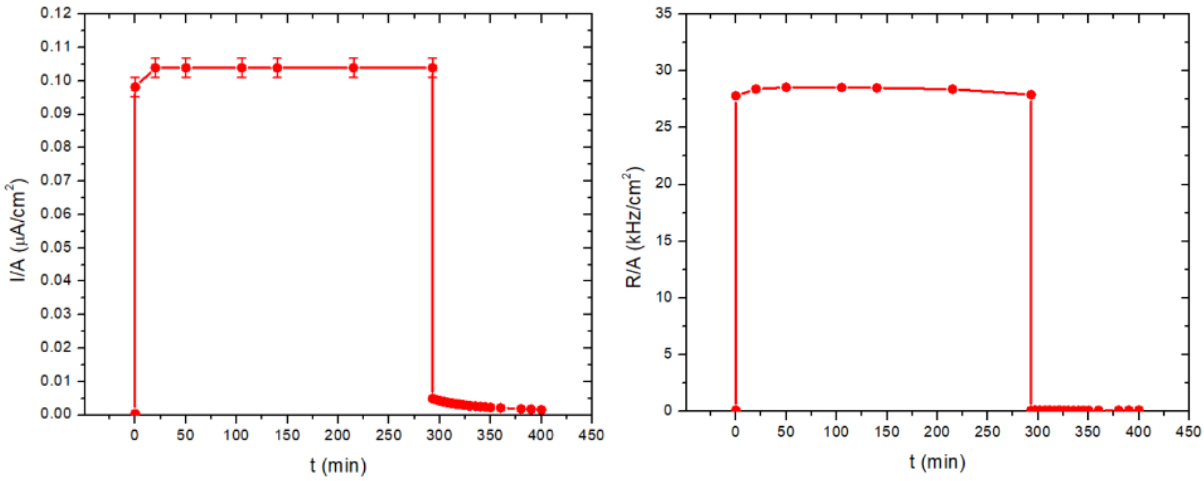

Figure 5.10: *The current (on the left side) and the counting rate (on the right) during the exposure.*

Each day after the exposure it was measured the dark current and the dark counting rate. Figure 5.11 shows the dark current decay curve after the exposure for the prototype with the gas exchange via diffusion (on the left side) and direct flow prototype (on the right side). It can be seen that the dark current of the direct flow prototype is slightly lower than the other prototype. The dark current for both prototypes decreases in time towards the values which they had before the irradiation, therefore a recovery process is observed.

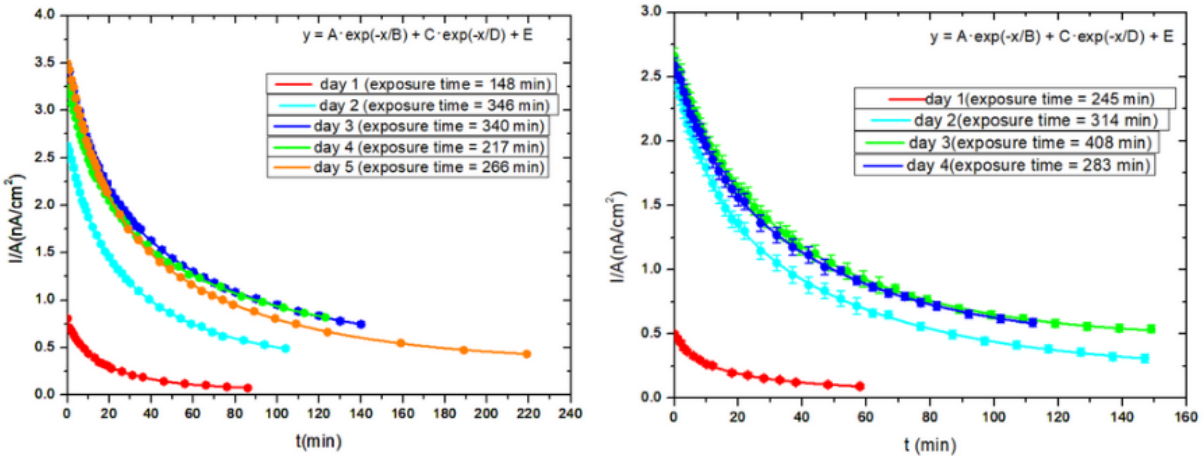

Figure 5.11: *The dark current for the diffusion gas exchange prototype (on the left side) and the dark current for the direct flow prototype (on the right side).*

The dark counting rate decay curves for both prototypes are showed in Figure 5.13. While the dark counting rate of the direct flow prototype decreases in time and a recovery process is observed, the dark counting rate for the prototype with gas exchange via diffusion exhibits a slight decrease for a short period of time after the irradiation but

increasing later on. Another interesting fact is that for both counters the dark counting rate increases as the counter accumulates charge.

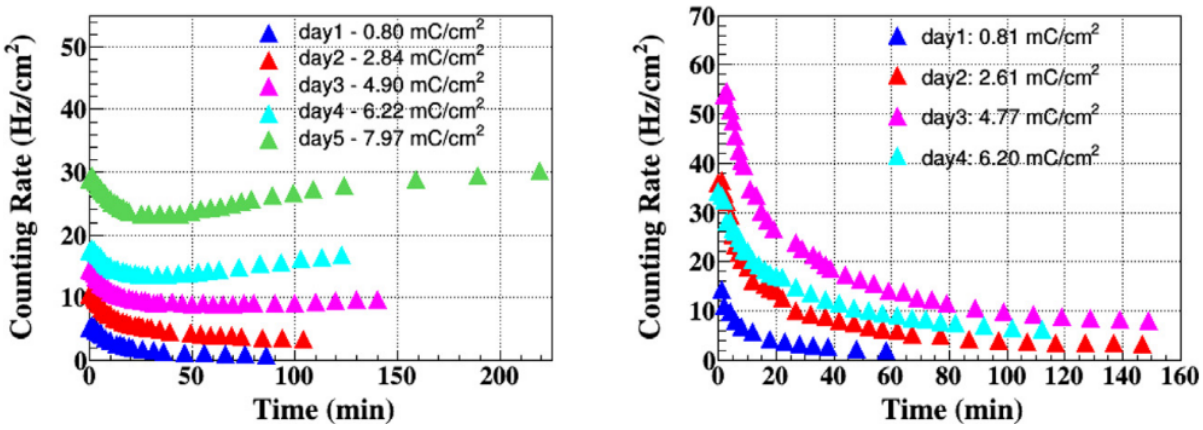

Figure 5.12: *The dark counting rate for the diffusion gas exchange prototype (on the left side) and the dark current for the direct flow prototype (on the right side). Figure taken from [51].*

In order to find new ways to reduce the observed ageing effects, the counter with a direct flow of the gas was irradiated for another 4 days, but this time it was exposed at different flow rates i.e. 2 l/h, 4 l/h, 6 l/h and 8 l/h.
Figure 5.13 depicts the decay curves of dark current on the left side and dark counting rate on the right side for different flow rates. Also, it can be observed that even if the counter accumulates charge, increasing the flow rate leads to a lower value of dark current and dark counting rate.

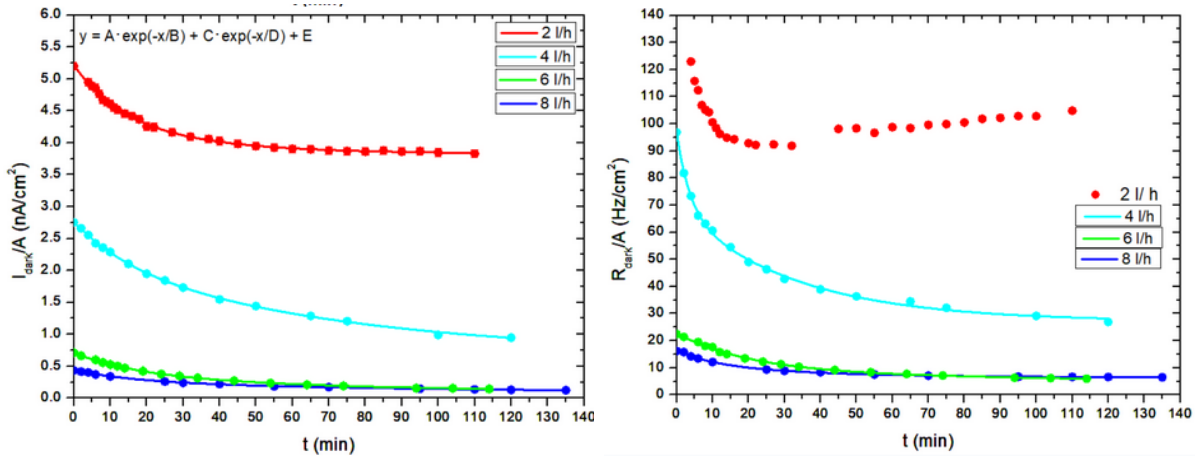

Figure 5.13: *The decay curves for the dark current (on the left side) and the dark counting rate (on the right side) for different gas flow rates.*

After the last exposure, the counter was tested, being operated in a self-triggered mode. The position along the strips was reconstructed using the time difference between the two ends of a strip for 32 strips. Figure 5.14 shows a 2D representation of the reconstructed position along the strip (y) as a function of strip number and on the right side is showed a 3D representation. It can be seen that the main source of the dark counting rate is localized around the spacer which was placed in the electric field. A gradient of dark counting rate along the spacer is also observed. A higher dark counting rate in the middle

of the counter can be explained by the fact that there is a lower gas exchange in the area around the spacer.

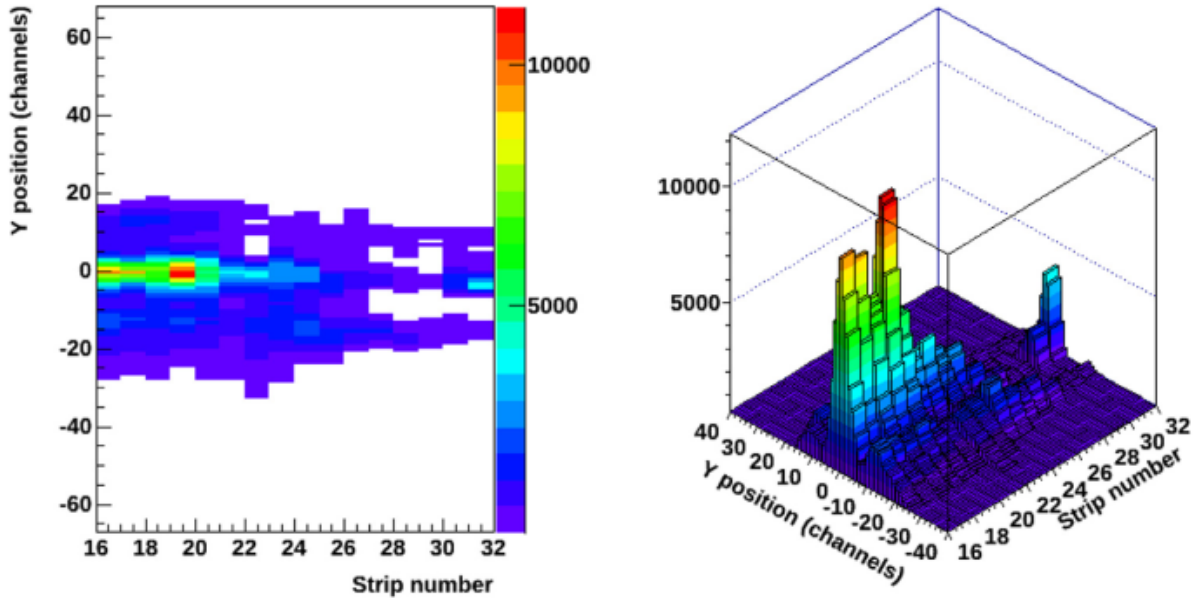

Figure 5.14: *The position along the strip as a function of the strip number. A higher dark counting rate is observed in the spacer region placed in the electric field. Also, it can be observed a gradient of the dark counting rate along the counter. Figure taken from [51].*

5.2 The 96 mm strip length MSMGRPC prototype

Based on the new architecture of MSMGRPC, a direct flow prototype of 96 mm was assembled and tested. In order to avoid the bending of the electrodes due to the high electric field, 2 spacers were placed inside the electric field and 2 spacers were placed outside the electric field as could be seen in Figure 5.1.
Using the same operating parameters i.e. the same working voltage and gas mixture, ageing tests of the new architecture of MSMGRPC were performed using 2 X-ray tubes. The logic electronic scheme was improved for these tests in order to have a better estimation of the counting rate.
A NINO chip readout a group of 8 strips and provide a logic OR if any strip from this group of 8 strips has a signal. After that a logic AND was performed between 2 logic OR signals delivered by the NINO chips of the two ends of a group of 8 strips. The output was recorded using a scaler with 4 down counters and a timer. The improvement brought by this new readout way can be seen in Figure 5.15 where a calibration curve in terms of the current as a function of the counting rate is depicted for a 96 mm strip length prototype. It can be seen that it has a linear behaviour for counting rates of up to 23 kHz/cm^2. Therefore, it turned out that the slight deviation from linearity which was observed at the calibration curve of the 56 mm strip length prototype (Figure 5.8) for counting rates above 15 kHz/cm^2 is only due to the logic electronic scheme where multiple logic OR between signals were performed which led to an underestimation of the counting rate for very high rates while the current was measured with high precision. Also, this idea is strengthened by the fact that there is no sign of pile-up effects which could be observed

on the oscilloscope at the maximum accessible counting rate (Figure 5.9.)

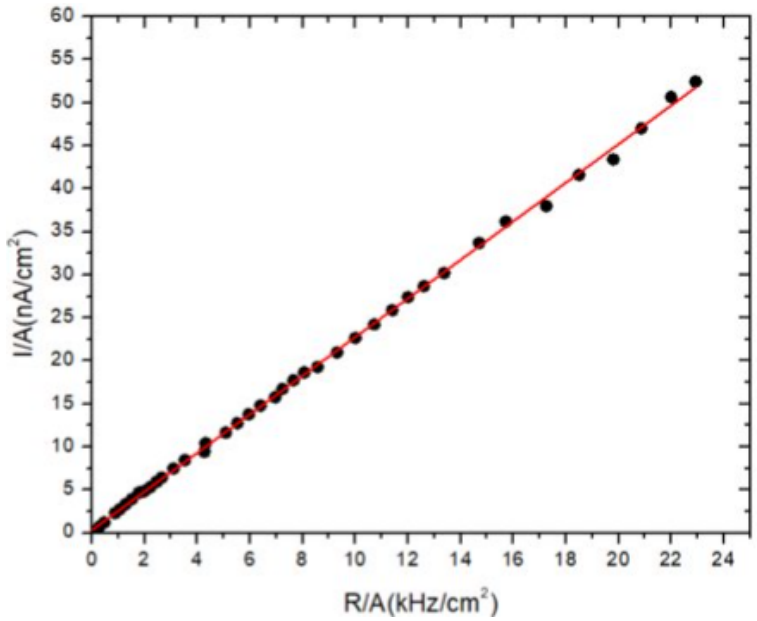

Figure 5.15: *The calibration curve in terms of current as a function of counting rate for the 96 mm strip length MSMGRPC prototype.*

Ageing studies were performed using the same experimental arrangement as for the previous prototype. The counter was exposed for 4 days at the maximum counting rate reached by using both X-rays tubes i.e. 23 kHz/cm^2. The accumulated charge for this period was 5.25 mC/cm^2. The current (on the left side) and the counting rate (on the right side) during the irradiation are showed in Figure 5.16. It can be seen that both current and counting rate are constant during the irradiation.

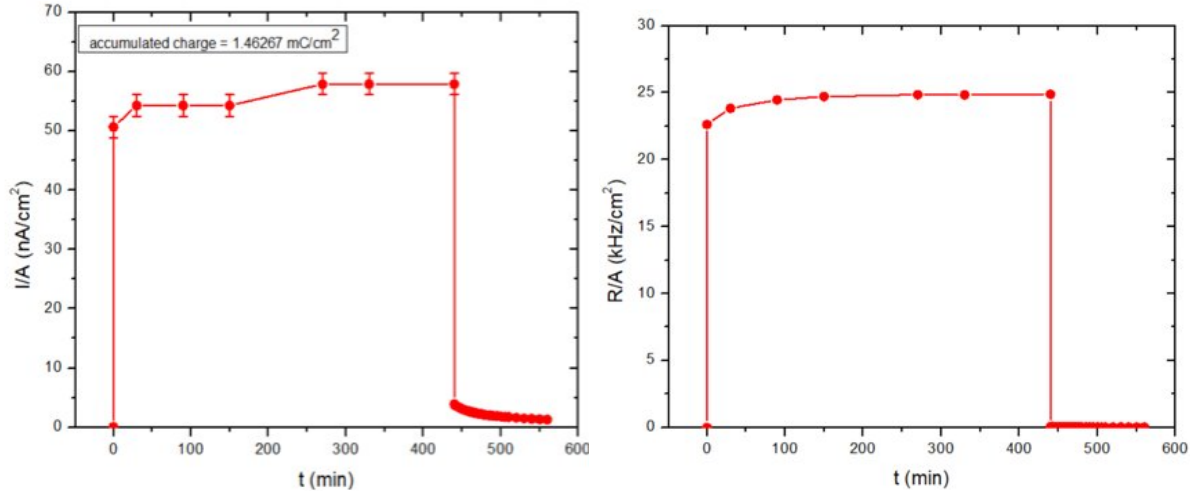

Figure 5.16: *The current (on the left side) and the counting rate (on the right side) during the irradiation for the 96 mm strip length MSMGRPC prototype.*

After each day of exposure, the dark current and dark counting were recorded. The same behaviour as for the previous prototype was observed. The decay curves of the dark

current (on the left side) and the dark counting rate (on the right side) are depicted in Figure 5.17. It can be observed that as the counter accumulates charge, the values of the dark current and the dark counting rate increase. Also, a jump in the dark counting rate was observed.

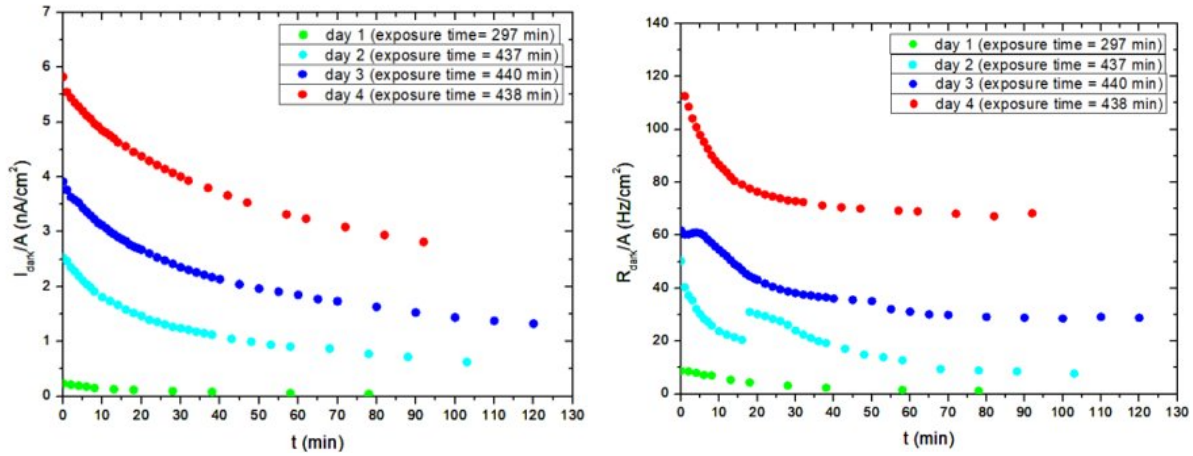

Figure 5.17: *The decay curves for the dark current (on the left side) and the dark counting rate (on the right side) for the 96 mm strip length MSMGRPC prototype.*

Figure 5.18 shows the evolution in time of the dark counting rate for each group of 8 strips readout by a NINO chip. It can be observed a gradient of the dark counting rate along the counter which could be correlated with a gas pollution effect such that the dark counting rate is low in the region where the gas enters through the counter and a higher dark counting rate is observed in the region where the gas gets out from the counter.

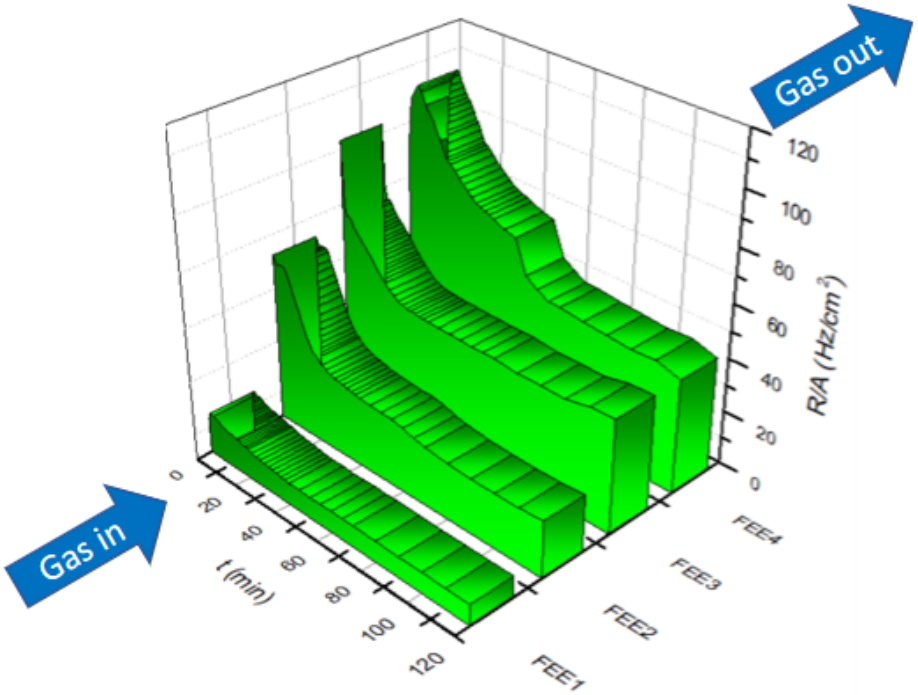

Figure 5.18: *A 3D representation of the dark counting rate for the 4 regions of the counter.*

This behaviour correlated with the observed trends of dark counting rate from Figure 5.17 where their values decrease towards the values measured before the irradiation turns out the idea of gas pollution of the counter and not the ageing of the glass plates.

In order to reduce the observed ageing effects, the counter was exposed for another 3 days but this time the gas flow rate was increased from 2 l/h to 4 l/h and afterwards to 6 l/h. The dark current (on the left side) and the dark counting rate (on the right side) are showed in Figure 5.19. It can be observed that even though the counter accumulates charge, the dark current and the dark counting rate decrease as the gas flow rate is increasing. The same behaviour was pointed out for the previous prototype i.e. 56 mm strip length.

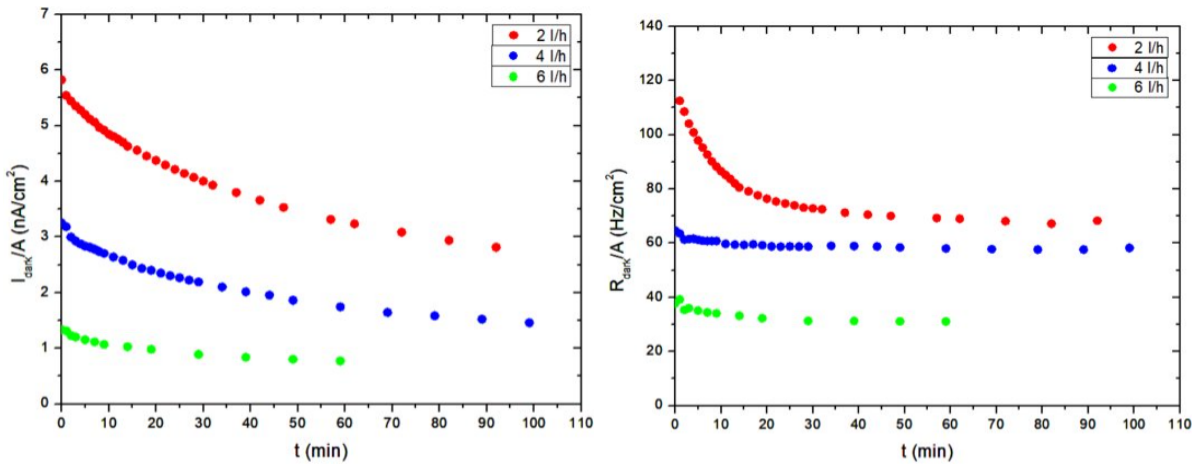

Figure 5.19: *The decay curves for the dark current (on the left side) and the dark counting rate (on the right side) for different gas flow rates for the 96 mm strip length MSMGRPC prototype.*

The recovery process, the gradient in the dark counting rate along the counter correlated with the gas exchange rate and the influence of the different gas flow rates on the performances of the counter leads to the idea of gas pollution and not to a degradation of the glass electrodes due to the ageing effects.
However, as could be seen in Figure 3.5 where is presented the architecture of the inner zone, the counters with 96 mm strip length are placed at larger polar angles than 56 mm strip length detectors, therefore the incident particle flux for this region will not exceed 10 kHz/cm^2. In order to study the ageing effects of this flux of particles over the counter, it was exposed at a counting rate of 12.6 kHz/cm^2 and after the exposure, the dark current and the dark counting rate were recorded. Figure 5.20 shows the decay curves for the dark current (on the left side) and the dark counting rate (on the right side) after the exposure at a counting rate of 23.3 kHz/cm^2 (red curves) and after the exposure at a counting rate of 12.6 kHz/cm^2 (green curves). It is worth mentioning that the gas flow rate during both exposures was 2 l/h. It can be seen that for the exposure at a realistic flux, the dark current and the dark counting rate have lower values and the parameters of the counter are not affected after the irradiation even if a flow rate of 2 l/h was used.

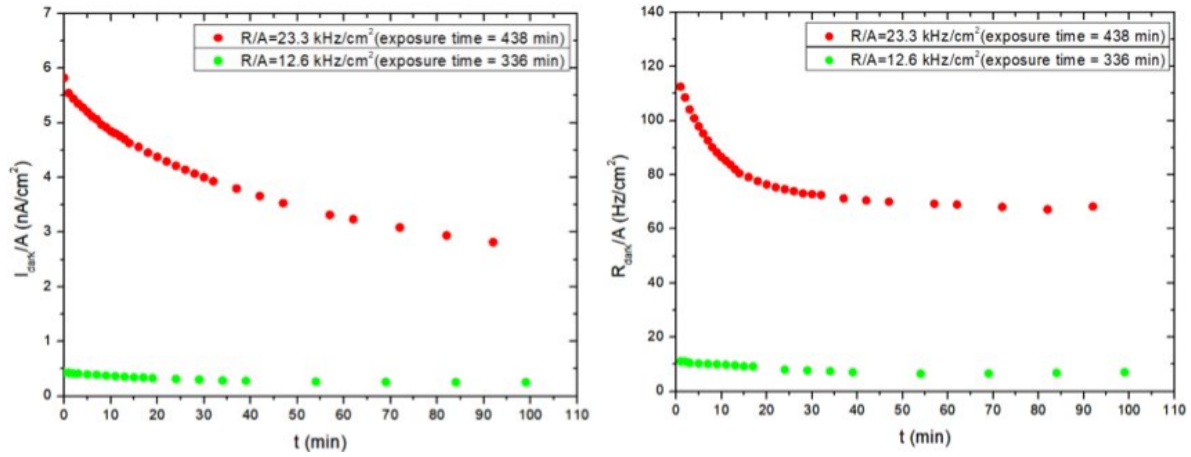

Figure 5.20: *The dark current (on the left side) and dark counting rate (on the right side) after exposure at* 23.3 kHz/cm^2 *(red curves) and* 10 kHz/cm^2 *(green curves).*

5.3 The 196 mm strip length MSMGRPC prototype

The last MSMGRPC prototype for the inner zone i.e. 196 mm strip length detector was assembled and tested using the same experimental arrangement as for the previous prototypes.
The incident particle flux for 196 mm strip length detectors from the inner zone is up to 6 kHz/cm^2. The counter was exposed at a slightly higher counting rate of 8 kHz/cm^2 for ageing tests. The gas flow rate was 2 l/h. Figure 5.21 depicts the current (on the left side) and the counting rate (on the right side) during the irradiation.

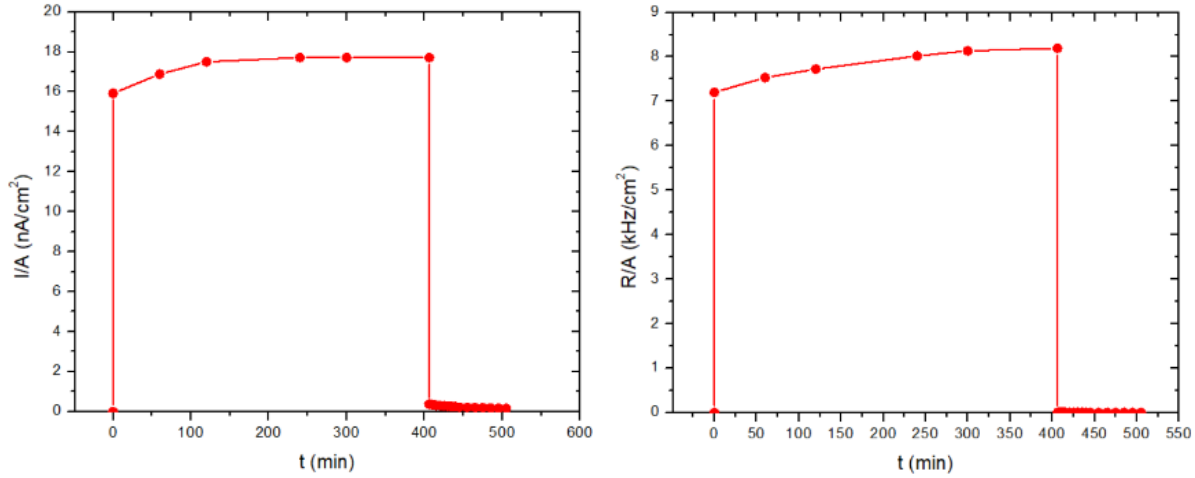

Figure 5.21: *The current (on the left side) and the counting rate (on the right side) during the irradiation for the 196 mm strip length MSMGRPC prototype.*

After the exposure, the dark current and the dark counting rate were recorded. Figure 5.22 depicts the decay curves for the dark current (on the left side) and the dark counting rate (on the right side). It can be seen that for this counting rate i.e. 8 kHz/cm^2 the values of the dark current and the dark counting rate are negligible. Also, a recovery process is observed.

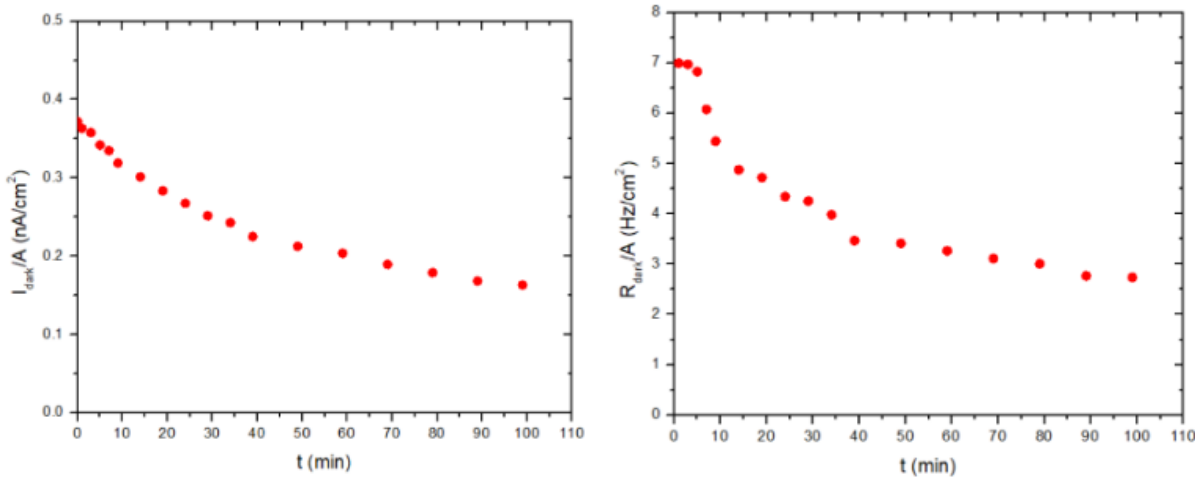

Figure 5.22: *The decay curves for the dark current (on the left side) and the dark counting rate (on the right side) for the 196 mm strip length MSMGRPC prototype.*

After the exposure, the counter was tested being operated in a self-triggered mode. Figure 5.23 depicts the position along the strips (y) as a function of the strip number. It can be seen that the main source of the dark counting rate is localized around the spacers placed in the electric field which can be explained by a lower gas exchange rate around the spacers.

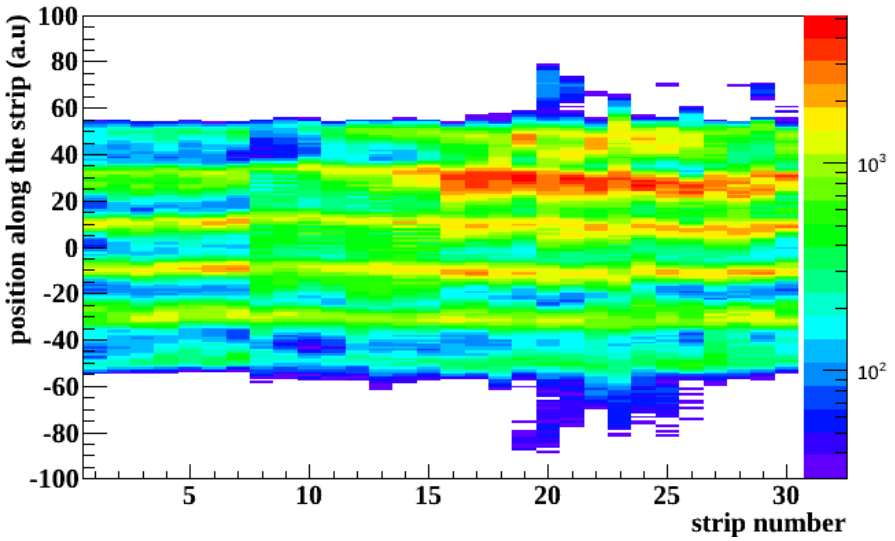

Figure 5.23: *The position along the strip as a function of the strip number.*

Conclusions

The future fixed target CBM experiment will study the Phase Diagram of strongly interacting matter at high baryon chemical potential, where the densities of the produced fireballs are 5-7 times higher than the normal nuclei, characteristic for the inner core of neutron stars, trying to look for phase transitions in the dense QCD matter and search for critical points of the Phase Diagram of QCD.
High-precision measurements of the rare diagnostic probes, the multi-differential analysis and the understanding of the observed trends in the experimental data require huge statistics. In order to achieve the required statistics in a reasonable time, the CBM experiment will run at interaction rates of up to 10 MHz for Au-Au collisions.
Charged hadrons identification will be performed using the time of flight method therefore, the information provided by both the ToF system based on MRPC (Multi-gap RPC) and the STS system which is placed in the magnetic field will be used.
The incident charged particle flux at 8 m from the target, has a strong dependence on the polar angle, therefore at the inner zone of the ToF system, counting rates of up to $4 \cdot 10^4$ $particles/cm^2 \cdot s$ will be reached. In order to fulfil the requirements for a qualitative PID, the detectors from the ToF system have to have an efficiency over 95%, a system time resolution better than 80 ps and to maintain their performances up to the highest counting rates reached at the low polar angles of the inner zone of the ToF system. Therefore, the inner zone of the CBM-ToF system will be based on state-of-the-art, high-rate, 2-dimensional position-sensitive, timing MSMGRPC detectors with low resistivity glass electrodes of different granularities i.e. 56/96/196 mm strip length.

The operation of the counters in a very high irradiation dose could affect their performances, therefore ageing tests were performed which showed the presence of a dark counting rate and a dark current after the irradiation. Also, depositions on both surfaces of the glass electrodes were observed.
CBM experiment will run in free streaming readout mode, hence the ageing effects of the counters have to be reduced at maximum such that to ensure the quality of the experimental data. In order to fulfil these requirements a new architecture of MSMGRPC was developed. In the actual architecture of MSMGRPC, the gas exchange between the gas gaps takes place via the diffusion process which leads to a low rate of gas exchange. Being well known that the polymerisation process is inversely proportional to the gas flow, the new architecture of MSMGRPC has a directed flow of the gas through the gas gaps which leads to higher gas exchange.
The ageing tests for the new architecture of MSMGRPC and for the previous one taken as reference were performed using 2 X-ray tubes. After the exposure, a dark counting rate and a dark current were observed for both prototypes whose values increase as the counter accumulates charge. While the dark current and dark counting rate for the new architecture decreases in time towards the values they had before the irradiation and a

recovery process is observed, the dark counting rate of the previous architecture of the counter where gas exchange takes place via the diffusion process increases in time towards a plateau and no recovery process is observed.
Further studies were performed for the new architecture of MSMGRPC in order to investigate the underlying physics of the recovery process and to find new ways for reducing the observed ageing effects. The influence of the gas flow rate during the irradiation on the recovery process was evidenced by the fact that increasing the gas flow rate leads to a lower value of dark current and dark counting rate even if the counter accumulates charge.
A gradient of the dark counting rate along the counter was observed which can be explained as a gas pollution effect. The main source of the dark counting rate is localized around the spacer region placed in the electric field, where the gas exchange rate is lower. Therefore, the observed ageing effects induced by the high-density avalanches due to high irradiation dose can be explained as a gas pollution effect and not as a deterioration of the glass electrodes.

The ageing tests were performed for all 3 prototypes of counters and the same behaviour in terms of ageing effects was observed for all of them. However, even if the total area of the spacer placed in the electric field is higher for the counters of 196 mm and 96 mm strip length than the 56 mm strip length prototype, they are exposed to a lower incident particle flux, therefore it turned out that the ageing effects are negligible for these prototypes for the expected incident particle flux.

Being observed that the main source of the dark counting rate is localized around the spacer region, further developments of the MSMGRPC are planned. Replacing the nylon fishing line spacers with discrete spacers distributed such that to avoid deformation of the glass plates due to the high electric field is expected to decrease the dark counting rate and the observed ageing effects.

The new architecture of the MSMGRPC fulfils the requirements for the inner zone of the CBM-ToF system not only in terms of time resolution and efficiency but also it demonstrated superior performances over the previous one in ageing tests due to the recovery process observed. Equipping the inner zone of the CBM-ToF system with this architecture of MSMGRPC and using a differential gas flow rate such that filling the counters with the highest granularity with a higher gas flow, will maintain the performances of the counters over the whole lifetime of the experiment foreseen to take data for 2 months a year for 10 years such that the physics goals of the CBM experiment to be achieved.

Bibliography

[1] W. Greiner et al. *Quantum chromodynamics*. Springer, 2007.

[2] R. Stock et al. *Relativistic Heavy Ion Physics*. Springer, 2011.

[3] K. Fukushima and T. Hatsuda. "The phase diagram of dense QCD". In: *Reports on Progress in Physics* 74.1 (Dec. 2010), p. 014001. DOI: 10.1088/0034-4885/74/1/014001.

[4] K. Fukushima and C. Sasaki. "The phase diagram of nuclear and quark matter at high baryon density". In: *Progress in Particle and Nuclear Physics* 72 (2013), pp. 99–154. DOI: https://doi.org/10.1016/j.ppnp.2013.05.003.

[5] B. Abelev et al. and (The ALICE Collaboration). "Upgrade of the ALICE Experiment: Letter Of Intent". In: *Journal of Physics G: Nuclear and Particle Physics* 41.8 (July 2014), p. 087001. DOI: 10.1088/0954-3899/41/8/087001.

[6] C. Yang. "The STAR beam energy scan phase II physics and upgrades". In: *Nuclear Physics A* 967 (2017), pp. 800–803. DOI: https://doi.org/10.1016/j.nuclphysa.2017.05.042.

[7] Ablyazimov et al. "Challenges in QCD matter physics –The scientific programme of the Compressed Baryonic Matter experiment at FAIR". In: *European Physical Journal A* 53 (Mar. 2017), 60(2017). DOI: 10.1140/epja/i2017-12248-y.

[8] B. Friman et al. *The CBM Physics Book-Compressed Baryonic Matter in Laboratory Experiments*. Springer-Verlag Berlin Heidelberg, 2010. ISBN: 978-3-642-13292-6.

[9] A. Andronic et al. "Hadron production in ultra-relativistic nuclear collisions: Quarkyonic matter and a triple point in the phase diagram of QCD". In: *Nuclear Physics A* 837.1 (2010), pp. 65–86. DOI: https://doi.org/10.1016/j.nuclphysa.2010.02.005.

[10] A. Pop M. Petrovici. "Features of hadronic and deconfined matter from AGS to LHC energies". In: (2022). DOI: 10.48550/ARXIV.2209.08828.

[11] *Interaction Rate as a function of center-of-mass energy*. https://github.com/tgalatyuk/interaction_rate_facilities.

[12] A. Senger and P. Senger. "Probing Dense QCD Matter: Muon Measurements with the CBM Experiment at FAIR". In: *Particles* 4.2 (2021), pp. 205–213. DOI: 10.3390/particles4020019.

[13] E. Grossi et al. "Soft pions and transport near the chiral critical point". In: *Phys. Rev. D* 104 (3 Aug. 2021), p. 034025. DOI: 10.1103/PhysRevD.104.034025.

[14] The CBM Collaboration. *ADDENDUM-Transition Radiation Detector 2D (TRD-2D)*. 2021.

[15] *GSI Helmholtzzentrum für Schwerionenforschung*. https://www.gsi.de/en/start/news.

[16] The CBM Collaboration. *Technical Design Report for the CBM-Time–of–Flight System (TOF)*. 2014.

[17] N. Herrmann. "CBM report". In: 41st CBM Collaboration Meeting, 2023.

[18] A. Shabunov A. Malakhov, ed. *Technical Design Report for the CBM Superconducting Dipole Magnet*. Darmstadt: GSI, 2013, 80 S.

[19] P. Senger. "Status of the Compressed Baryonic Matter experiment at FAIR". In: *Int. J. Mod. Phys. E* 29.02 (2020), p. 2030001. DOI: 10.1142/S0218301320300015.

[20] The CBM Collaboration. *Technical Design Report for the CBM-Micro-Vertex Detector (MVD)*. 2021.

[21] J. Heuser et al., ed. *[GSI Report 2013-4] Technical Design Report for the CBM Silicon Tracking System (STS)*. Darmstadt: GSI, 2013.

[22] C. Höhne et al., ed. *Technical Design Report for the CBM Ring Imaging Cherenkov Detector*. CBM Technical Design Reports. 2013.

[23] S. Chattopadhyay et al., ed. *Technical Design Report for the CBM : Muon Chambers (MuCh)*. Darmstadt: GSI, 2015.

[24] The CBM Collaboration. *Technical Design Report for the CBM-The Transition Radiation Detector(TRD)*. 2018.

[25] P.Senger et al. *CBM Progress Report 2021*. Tech. rep. 2022. 2022, 239 p. DOI: 10.15120/GSI-2022-00599. URL: https://repository.gsi.de/record/246663.

[26] I. E. Korolko et al. "The CBM ECAL". In: *Journal of Physics: Conference Series* 798.1 (Jan. 2017), p. 012164. DOI: 10.1088/1742-6596/798/1/012164.

[27] F. Guber et al., ed. *Technical Design Report for the CBM Projectile Spectator Detector (PSD)*. Darmstadt: GSI, 2015.

[28] Anna Senger. In: *The CBM collaboration* ().

[29] C. Lippmann. "Particle identification". In: *Nuclear Instruments and Methods in Physics Research Section A: Accelerators, Spectrometers, Detectors and Associated Equipment* 666 (2012), pp. 148–172. DOI: https://doi.org/10.1016/j.nima.2011.03.009.

[30] M. C. S. Williams. In: 39.12 (Oct. 2012), p. 123001. DOI: 10.1088/0954-3899/39/12/123001.

[31] M. Petris. "RPC - general presentation". In: 2010.

[32] M. Petris. "High rate, high time resolution, 2D-position sensitive and aging effect suppression Multi-Strip Multi-Gap Resistive Plate Counter". In: 2022.

[33] P. Fonte M. Abbrescia V. Peskov, ed. *Resistive Gaseous Detectors: Designs, Performance, and Perspectives*. Wiley-VCH, 2018.

[34] M. Petriş et al. "Time and position resolution of high granularity, high counting rate MRPC for the inner zone of the CBM-TOF wall". In: *Journal of Instrumentation* 11.09 (Sept. 2016). DOI: 10.1088/1748-0221/11/09/C09009.

[35] M. Petrovici et al. "A large-area glass-resistive plate chamber with multistrip readout". In: *Nuclear Instruments and Methods in Physics Research Section A: Accelerators, Spectrometers, Detectors and Associated Equipment* 487.3 (2002), pp. 337–345. DOI: https://doi.org/10.1016/S0168-9002(01)02192-1.

[36] W. R. Leo. *Techniques for nuclear and particle physics experiments: a how-to approach*. Springer-Verlag Berlin Heidelberg GmbH, 1994.

[37] G. F. Knoll. *Radiation Detection and Measurement*. John Wiley and Sons, Inc., 2010.

[38] F. Sauli. *Gaseous Radiation Detectors: Fundamentals and Applications*. Cambridge University Press, 2014.

[39] *ALICE Time-Of-Flight system (TOF): Technical Design Report*. Technical design report. ALICE. CERN, 2000.

[40] M.C.S Williams et al. E C. Zeballos. "A new type of resistive plate chamber: The multigap RPC". In: *Nuclear Instruments and Methods in Physics Research Section A: Accelerators, Spectrometers, Detectors and Associated Equipment* 374.1 (1996), pp. 132–135. DOI: https://doi.org/10.1016/0168-9002(96)00158-1.

[41] M.C.S Williams et al. "The multigap resistive plate chamber as a time-of-flight detector". In: *Nuclear Instruments and Methods in Physics Research Section A: Accelerators, Spectrometers, Detectors and Associated Equipment* 456.1 (2000), pp. 16–22. ISSN: 0168-9002. DOI: https://doi.org/10.1016/S0168-9002(00)00954-2.

[42] M. Petrovici et al. "Multistrip multigap symmetric RPC". In: *Nuclear Instruments and Methods in Physics Research Section A: Accelerators, Spectrometers, Detectors and Associated Equipment* 508.1 (2003), pp. 75–78. DOI: https://doi.org/10.1016/S0168-9002(03)01280-4.

[43] M. Kiš et al. "A Multi-strip Multi-gap RPC Barrel for Time-of-Flight Measurements". In: *Nuclear Instruments and Methods in Physics Research Section A: Accelerators, Spectrometers, Detectors and Associated Equipment* 646.1 (2011), pp. 27–34. DOI: https://doi.org/10.1016/j.nima.2011.02.076.

[44] Jingbo Wang et al. "Development of high-rate MRPCs for high resolution time-of-flight systems". In: *Nuclear Instruments and Methods in Physics Research Section A: Accelerators, Spectrometers, Detectors and Associated Equipment* 713 (2013), pp. 40–51. DOI: https://doi.org/10.1016/j.nima.2013.02.036.

[45] M. Petris et al. "PERFORMANCE OF THE MSMGRPC WITH THE HIGHEST GRANULARITY OF THE CBM-TOF WALL IN COSMIC RAY TESTS". In: *Romanian Journal of Physics* 66.305 ((2021).

[46] M. Petris et al. "A METHOD TO ADJUST THE IMPEDANCE OF THE SIGNAL TRANSMISSION LINE IN A MULTI-STRIP MULTI-GAP RESISTIVE PLATE COUNTER". In: *Romanian Journal of Physics* 63.901 ((2018).

[47] A. Senger. "Design simulations of beam pipe and radiation studies for the CBM experiment". In: *CBM-TN-18001* ((2018).

[48] M. Petrovici et al. “Ageing studies of Multi-Strip Multi-Gap Resistive Plate Counters based on low resistivity glass electrodes in high irradiation dose”. In: *Nuclear Instruments and Methods in Physics Research Section A: Accelerators, Spectrometers, Detectors and Associated Equipment* 1024 (2022), p. 166122. DOI: https://doi.org/10.1016/j.nima.2021.166122.

[49] H. Yasuda. “New insights into aging phenomena from plasma chemistry”. In: *Nuclear Instruments and Methods in Physics Research A* (2010).

[50] M. Petriş et al. “High time resolution, two-dimensional position sensitive MSM-GRPC for high energy physics experiments”. In: *Nuclear Instruments and Methods in Physics Research Section A: Accelerators, Spectrometers, Detectors and Associated Equipment* 1045 (2023), p. 167621. DOI: https://doi.org/10.1016/j.nima.2022.167621.

[51] M. Petris et al. “Aging suppression, high time resolution and 2D-position sensitive Multi-Strip Multi-Gap Resistive Plate Counter for high rate experiments”. In: *Nuclear Instruments and Methods in Physics Research Section A: Accelerators, Spectrometers, Detectors and Associated Equipment* 1049 (2023), p. 168098. DOI: https://doi.org/10.1016/j.nima.2023.168098.

[52] The CBM Collaboration. *mCBM@SIS18*. 2017.

[53] M. Ciobanu et al. “New Models of PADI, an Ultrafast Preamplifier–Discriminator ASIC for Time-of-Flight Measurements”. In: *IEEE Transactions on Nuclear Science* 68.6 (2021), pp. 1325–1333. DOI: 10.1109/TNS.2021.3073487.

[54] F. Anghinolfi et al. “NINO: an ultra-fast and low-power front-end amplifier/discriminator ASIC designed for the multigap resistive plate chamber”. In: *Nuclear Instruments and Methods in Physics Research Section A: Accelerators, Spectrometers, Detectors and Associated Equipment* 533.1 (2004), pp. 183–187. DOI: https://doi.org/10.1016/j.nima.2004.07.024.